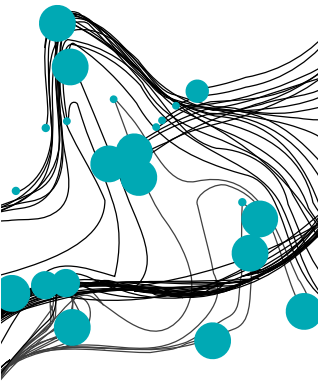

RAM ROBOTICS AND MECHATRONICS

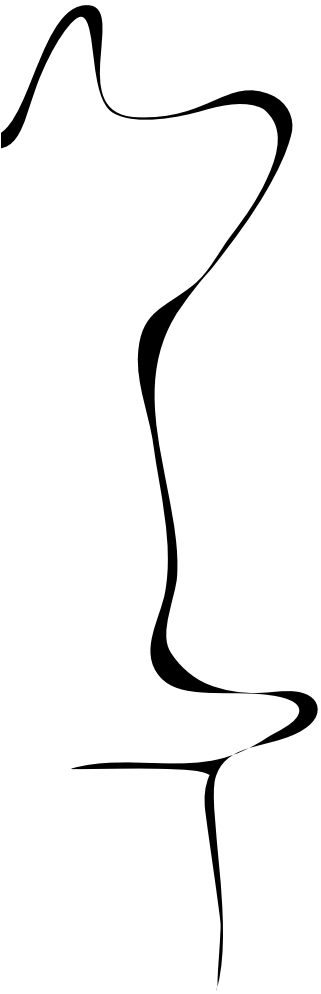

AERODYNAMIC INTERFERENCES FOR THE OMNIMORPH AERIAL VEHICLE

R.J. (Ralph) Brantjes

MSC ASSIGNMENT

Committee:
prof. dr. ir. G.J.M. Krijnen
prof. dr. ir. A. Franchi
C. Gabellieri, Ph.D
dr. ing. G. Englebienne

february, 2024

008RaM2024
Robotics and Mechatronics
EEMCS
University of Twente
P.O. Box 217
7500 AE Enschede
The Netherlands

UNIVERSITY OF TWENTE. | TECHMED CENTRE UNIVERSITY OF TWENTE. | DIGITAL SOCIETY INSTITUTE

Summary

With advancements in control, electronics, and batteries, drones have gained more and more popularity over the years. Constant research is being done into new ways to use them for various interaction, surveillance, and manipulation tasks. This thesis considers a new drone platform called the OmniMorph. The OmniMorph is an octorotor with a single servo motor that can tilt all the rotors simultaneously. This servo enables the OmniMorph to change its configuration (morph) between an energy-efficient and omnidirectional configuration. Due to the placement of the rotors, the OmniMorph is subjected to aerodynamic effects between the rotors (aerodynamic interference). This thesis considers these effects and proposes different solutions to minimize aerodynamic interference. The accuracy of the wrench execution and the most energy-efficient tilt angle of the rotors is investigated. From the experiments, we find that increasing the distance between the rotors could potentially be a solution to minimize the aerodynamic interference. Higher tilt angles and lower rotor velocities result in better accuracy of the wrench execution. The most energy-efficient tilt angle for hovering is still with all rotors pointing upwards. In the end, additional recommendations are given for future research into the effects of aerodynamic interference and a more complex model than the current standard UAV model is discussed.

Acknowledgements

Several people have helped me out a lot throughout this thesis. I would like to take the opportunity to thank each of them.

First of all, I would like to thank Antonio Franchi for allowing me to work on the OmniMorph project, for taking the time to help me out whenever I had questions, and for guiding me along the way. I would also like to thank him for providing creative and different ways to think about problems and solutions during the aerial robotics meetings.

I would like to thank Chiara Gabellieri for picking up the daily supervisor role and helping me throughout the middle and end of the thesis. I would also like to thank her for the opportunity to perform experiments and gather data that was used in the publication of the paper about the OmniMorph. I am really glad to have had her as a daily supervisor because she made me feel like a valued member of the group and included me in the decisions and conversations about the OmniMorph project.

I would also like to thank Quentin Sable for helping me out so much with everything mechanical. From making the setup, helping me build the clone of the OmniMorph, and 3D-printing all the necessary parts. Whenever I needed something, Quentin was always ready with a solution.

I would like to thank Youssef Aboudorra for helping me out during the start of my thesis and providing me with the necessary information to start.

I would like to thank Amr Afifi for helping me understand the software part of the thesis and guiding me through the times I was stuck on software-related issues.

Last of all, I would like to thank all the other people around me who helped me out with everything else during my thesis. First and foremost, my girlfriend Sarah who was always patient with me when I was busy and was always prepared to help me with anything I needed. My parents and the rest of my family, who provided support whenever I needed it. And of course, all my friends who provided me with good times and relaxation whenever I felt stressed.

List of Figures

Contents

1 Introduction

In this thesis, we will be discussing the aerodynamics of the OmniMorph. This chapter will serve as an introduction to the thesis. It will start by giving some context to the thesis. It will then discuss related literature and previous work done on the platform considered in this thesis. It will then show the contributions this thesis has made and then mention the goals set for the overall project and this thesis.

1.1 European Aerial-Core Project

This thesis has been instigated through the Robotics and Mechatronics Group (RaM)[1] at the EEMCS faculty of the University of Twente and is motivated by the use cases of the European Aerial-Core project[2]. Aerial-Core consists of universities and organizations researching advanced technologies in the unmanned aerial vehicle (UAV) space. A representation of what the Aerial-Core project stands for can be seen in Figure 1.1. The goals of Aerial-Core are as follows:

1. Improve the cognitive capabilities of the UAVs. This entails, among other things, the perception, data fusion, and reaction time of the UAVs.
2. Use morphing (changing the configuration) of the platform to its advantage. This can, for example, be used to toggle between the most efficient flight mode and the most precise flight mode, improving both the flight time and the accuracy of the overall UAV.
3. Use aerial manipulation to enable the usage of the UAV to change its environment through different maneuvers such as grabbing, pushing, or pulling.
4. Be able to interact with people to help them perform certain tasks safely. This is called aerial co-working.
5. Use the UAVs for easy inspection and maintenance of large infrastructures.

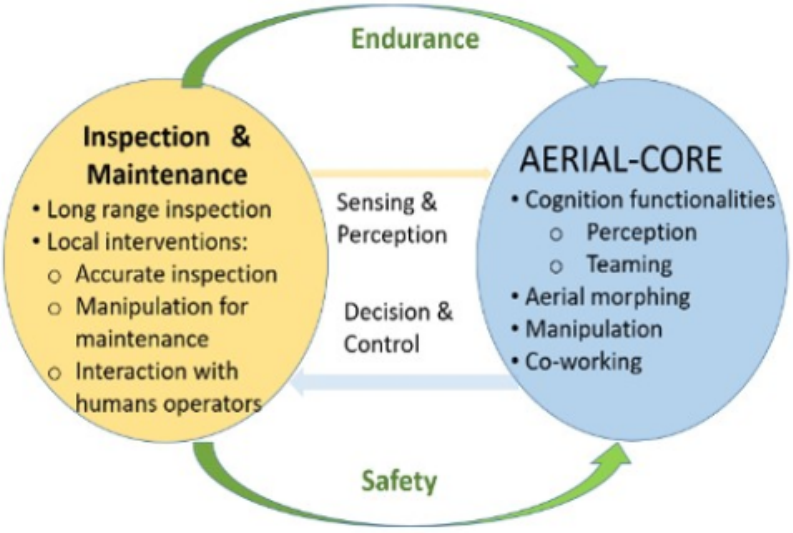

Figure 1.1: The Aerial-CORE project tenets from their website Ollero (2023). (Credit Aerial-Core)

[1] https://www.ram.eemcs.utwente.nl/
[2] https://aerial-core.eu/

(a) Human-robot cooperation.

(b) Electrical line inspection and maintenance.

Figure 1.2: Different tasks performed by UAVs. Images from Ollero (2023) (Credit: Aerial-Core).

The practical value of the Aerial-Core project is to use different ideas for UAVs in situations where certain difficult tasks can be alleviated with the help of a UAV. Some examples can be seen in Figure 1.2 where Figure 1.2a shows how the human-robot interaction can be used in situations where a human can make use of a drone to fetch and hand over tools. The second example in Figure 1.2b shows how a drone can be used to maintain and inspect power lines without needing a human to climb up to the electrical lines.

The Aerial-Core project considers many different types of UAVs. The one considered in this thesis is called the OmniMorph. It is a UAV with omnidirectional (OD) capabilities and can change the orientation of its propellers (morphing). A more in-depth description of the platform will be given later in this thesis. The thesis focuses mainly on the second objective of the Aerial-Core project. Namely, exploiting the morphing capabilities of the OmniMorph to trade off efficiency for omnidirectional capabilities.

1.2 Context

The European Aerial-Core project is not the only group researching and innovating on the UAV front. Due to the increase in performance and the reduction of size and weight of batteries and microprocessors, the use of UAVs is becoming increasingly attractive for a multitude of other applications Wargo et al. (2014). Currently, there are two primary types of UAVs.
Fixed-wing UAVs, the first type, are often used for long-range applications, with their plane-like appearance benefiting from wings that are able to generate lift. Additionally, fixed-wing UAVs can carry more payload than their multi-rotor counterparts Panagiotou and Yakinthos (2020). Fixed-wing UAVs are used in typical military applications and for civic applications such as fire detection, search and rescue, and many more. Khan et al. (2017) created a fixed-wing UAV possessing LiDAR technology to map the Amazonian rainforest for archeological purposes.
The second distinctive form of UAVs is the category of multi-rotor aerial vehicles, which are also referred to as vertical take-off and landing UAVs (VTOL). This is the category that the OmniMorph belongs to. As the name suggests, this type of UAV possesses multiple rotors. This category of UAVs has the benefit of hovering and maneuverability. This opens up a different realm of possibilities. The current use of UAVs ranges from agricultural applications such as surveillance of crops Lottes et al. (2017) to more civic applications such as traffic monitoring Mohammed et al. (2014) and disaster management Erdelj et al. (2017). The downsides of the multi-rotor UAV are the flight time and the carrying capacity. This type of platform has to make a well-considered choice between multiple design parameters such as the weight of the platform, the battery capacity, and more Delbecq et al. (2020). Currently, the most used form of multi-rotor UAV is the quadrotor.

Beyond these categories, hybrid versions of UAVs have been created which combine the ability of VTOLs for take-off and landing and the efficiency of the fixed-wing UAVs to travel long distances Saeed et al. (2018). As the technology improves, more creative uses for UAVs have been conceived, such as the use of UAVs for aerial manipulation using a rod or an arm to manipulate the environment Nikou et al. (2015) or swarm robotics Franchi et al. (2012) (using a multitude of drones working together). Companies such as DJI[3] offer a range of commercial drones for entertainment and video.
With UAVs being used for more and more applications, growing research is done pertaining to the optimal configuration of the UAV for the required task at hand Hamandi et al. (2021).

1.3 Related literature

Among many different types of UAVs, many different designs are proposed in the literature. The Omnimorph possesses both omnidirectional capabilities and morphing capabilities. There are several papers related to these two types of UAV behavior.

1.3.1 Omni-directionality

Omni-directional UAVs or ODARs (omnidirectional aerial robots) are still a recent occurrence in literature, with Park et al. (2016) being the earliest found, which was published in 2016. Park et al. (2016) consists of a hexarotor design with bidirectional propellers. A representation of the proposed design can be seen in Figure 1.3a.
The same authors as Park et al. (2016) proposed a newer version of the omnidirectional design in Park et al. (2018) in 2018. This version looks similar to 1.3a but possesses eight bidirectional propellers. The drone can be seen in Figure 1.3c. Where Park et al. (2016) focused only on making the design possible, Park et al. (2018) tries to optimize different aspects of UAV design. It is focused on optimizing the minimum force and torque necessary for the desired position and attitude of the UAV.
Allenspach et al. (2020) is a noteworthy paper presenting an omnidirectional platform which is also able to tilt its propellers actively. Similarly to the OmniMorph, it can transform from an energy-efficient configuration to an agile, omnidirectional configuration. The platform uses a hexarotor design but possesses 12 propellers.

1.3.2 Morphing

UAVs with morphing designs are used for a variety of applications. Tilting propellers is one of the most common ways of morphing. One of the first in the literature to propose such a design was Ryll et al. (2012) in 2012 with a quadrotor with tilting propellers. This idea was presented as a solution to the problems occurring with quadrotors' underactuated (UA) configuration. Section 2.2.4 gives more information on actuation. Kim et al. (2021) uses the morphing capability of a quadrotor in combination with a pickup mechanism to optimize payload transportation. Falanga et al. (2019) has a similar design to Kim et al. (2021). In the case of Falanga et al. (2019), the morphing capabilities are used to squeeze through harder-to-access locations and fly in multiple configurations.
Zhao et al. (2018) created the multilink morphing 'dragon' UAV seen in Figure 1.4a. This configuration is meant to be able to navigate complex environments and, in the future, manipulate objects.
A noteworthy design possessing both morphing capabilities and omnidirectional capabilities is the Voliro Kamel et al. (2018). A depiction of the Voliro is shown in Figure 1.4b. The UAV consists of a hexarotor with unidirectional propellers, which are able to tilt in such a fashion that the platform is omnidirectional. This platform has been improved over time and has become

[3] https://www.dji.com/nl

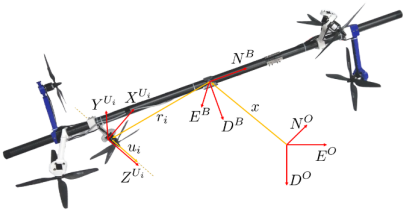

(a) First version of the ODAR. This version is a hexarotor. Credit: Park et al. (2016) ©IEEE.

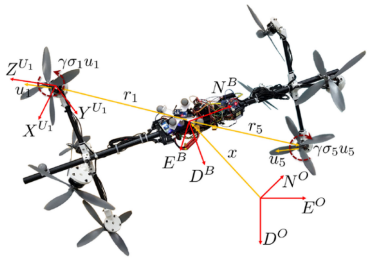

(b) Second version of the ODAR. This version is an octorotor. Credit: Park et al. (2018) ©IEEE.

(c) Omni-directional tiltrotor design. Credit: Allenspach et al. (2020) ©SAGE Publications.

Figure 1.3: Examples found in literature pertaining to the omnidirectional capabilities of the OmniMorph.

the Voliro-T seen in Figure 1.4c. This is a commercial platform possessing five rotors, which uses its modular end-effectors for inspection and similar tasks in hard-to-reach places.

1.3.3 OmniMorph inspiration

The OmniMorph is most related to the platforms of Brescianini and D'Andrea (2018) and Ryll et al. (2022). The omnidirectional platform of 1.5a has a design that looks similar to the OmniMorph. Similarly to Park et al. (2018), Brescianini and D'Andrea (2018) is an octo-rotor design with bidirectional fixed tilt propellers. The UAV can be seen in Figure 1.5a. The purpose of the design of Brescianini and D'Andrea (2018) is to maximize the UAV's agility while rendering its characteristics almost rotationally invariant. While Brescianini and D'Andrea (2018) is similar in terms of looks, the single servo design of the OmniMorph is similar to Ryll et al. (2022). The FAST-Hex is a hexarotor platform that uses a tilting mechanism to transition from an under-actuated to a fully-actuated configuration. A representation of the FAST-Hex can be seen in Figure 1.5b. Similar to the FAST-Hex, the OmniMorph uses a single servo motor to actively tilt its propellers to change configuration from an energy-efficient configuration to an agile configuration.

1.4 The OmniMorph

The OmniMorph is a platform that is being developed within the RaM research group at the University of Twente. The OmniMorph is a novel design of an octo-rotor UAV with an additional servo motor. The eight rotors are spaced equidistant from each other and are equidistant from the centre of mass (CoM), with four top rotors and four bottom rotors. A representation of the OmniMorph can be seen in Figure 1.6. The OmniMorph possesses bidirectional propellers, enabling the rotors to spin in both directions. The servo motor is able to tilt all the propellers simultaneously. This is how the platform is able to 'morph'. The goal of the OmniMorph is to exploit this morphing capability to trade off the energy efficiency of upwards-facing propellers

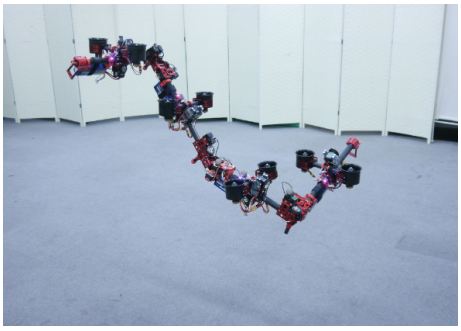

(a) DRAGON: Dual-rotor embedded multilink Robot with the Ability of multi-deGree-of-freedom aerial transformatiON Zhao et al. (2018) ©IEEE.

(b) Voliro prototype. Credit: Kamel et al. (2018) ©IEEE.

(c) Voliro-T Credit: Voliro AG.

Figure 1.4: Different instances in literature of platforms possessing morphing capabilities.

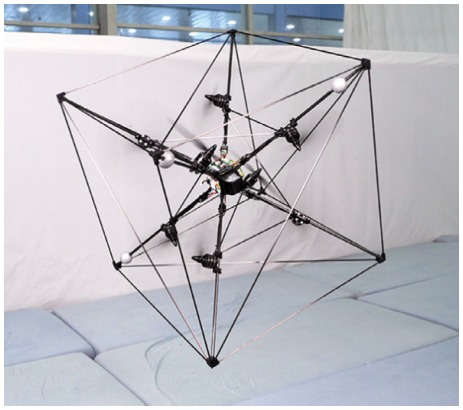

(a) Omni-directional octorotor designed by Brescianini and D'Andrea (2018). With permission from ©Elsevier.

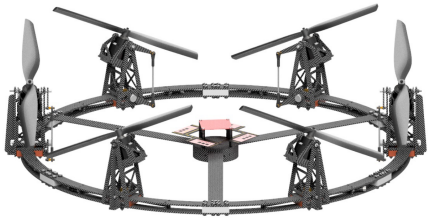

(b) FAST-Hex: an actively tilting hexarotor. Credit: Ryll et al. (2022) ©IEEE.

Figure 1.5: The two platforms from which the OmniMorph is most inspired. It uses the omnidirectional octo-rotor design from (a) and the single servo motor with an actively tilted propeller mechanism from (b).

for the accuracy and omnidirectionality of tilted propellers. The OmniMorph is, in its omnidirectional configuration, able to compensate for gravity in all orientations, which enables it to perform complex manoeuvres such as flying upside down.

Figure 1.6: Model of the OmniMorph. Left: OmniMorph in the most energy-efficient rotor configuration by pointing all rotors directly upwards. Right: OmniMorph in the omnidirectional configuration, enabling it to hold its own weight in all possible poses. Credit: Aboudorra et al. (2024)

1.5 Previous work

Previous work has been done on the OmniMorph during the master thesis of Kevin Jeulink Jeulink (2023). Kevin's main work was to create an NMPC (Nonlinear Model Predictive Control) controller for the OmniMorph. This was done in MATLAB simulations using MATMPC Chen et al. (2019). The NMPC can be simulated using MATLAB and Simulink, which shows that the OmniMorph can follow trajectories and perform complicated manoeuvres without becoming unstable. Kevin Jeulink (2023) also explored the robustness of the NMPC algorithm by injecting minor deviations in the model of the OmniMorph.
The omnidirectionality (OD) of the platform has been explored previously, as seen in Aboudorra et al. (2023). The OmniMorph can theoretically achieve OD at a rotor tilt angle of 37 degrees. Aboudorra et al. (2023) also looked at the power usage of the OmniMorph, the maximum additional mass that the tilting mechanism could add, and the control of the OmniMorph. Some additional questions were brought up during the reviewing process of Aboudorra et al. (2023) about the aerodynamic effects of spinning rotors on each other.

1.6 Thesis contribution

- This thesis gives an insight into the difference between the standard theoretical simplified UAV models and the physical application of the OmniMorph platform.
- A clone of the OmniMorph was built for future steps, such as implementing a tilting mechanism.
- The OmniMorph has been evaluated at different tilt angles. This was not done previously for the physical platform.
- The effects of complex aerodynamic effects on the OmniMorph are explored, and the differences between aerodynamic effects being present and being absent are brought into question and quantified.
- We look at the effects for which the standard linear model holds and for which additional nonlinear effects need to be considered when using the real OmniMorph platform.
- Some of the data gathered during this thesis was used for the publication Aboudorra et al. (2024) within the Journal of Intelligent & Robotic Systems (JINT).

- The experiment results have been used in a proposed conference paper Bazzana et al. (2024) to validate a generalized model for the propeller force accounting for the cross-influence of multi-rotor aerial systems.

1.7 Problem description

1.7.1 Goal

The final goal of the OmniMorph project is to create an omnidirectional, efficient morphing platform for outdoor use that is able to perform physical interaction tasks. From experiments done on the platform, it has been established that aerodynamic effects occur between the different rotors of the OmniMorph. This thesis aims to use a basic prototype of the OmniMorph and gain an understanding of the aerodynamic interaction between the rotors (aerodynamic interference) of the physical platform to quantify these effects. This knowledge about the OmniMorph platform's aerodynamics enables accounting for these effects once the OmniMorph is able to fly in the future.

1.7.2 Research questions

To quantify the effects due to the aerodynamics, the following research questions have been formed:

- How accurate is the wrench execution when the tilt angle (α) is changed with the wrench mechanism? Is some alpha better and more accurate?
- Is there a design modification that would lead to an optimal value of alpha corresponding to a lower value of the control input at hovering compared to the optimal alpha of the current prototype?

1.7.3 Thesis outline

This thesis will continue by explaining the necessary background information needed. Then, information is given about the aerodynamic effects taking place on the OmniMorph. After this, the design of the physical platform is discussed. With the knowledge of the background and the platform, the different experiments performed on the OmniMorph during this thesis are shown and the results are discussed. Last of all, the research questions are answered in the conclusion, and recommendations are given.

2 Fundamental background for the OmniMorph

This chapter gives the necessary background to get a holistic understanding of the OmniMorph, and a general description of the modeling of UAVs is given. We first introduce the notation used throughout this thesis. This includes all the essential coordinate frames. The modelling will start with the force and moment produced by a propeller. These forces and moments are transformed to the body and influence the dynamics. The actuation of the OmniMorph is introduced, and the power exerted by the rotors is explained.

2.1 Notation

The following notation will be used throughout this thesis:

- **Bold** lowercase text is used for the representation of vectors e.g. $\boldsymbol{f}$
- **Bold** uppercase text is used for the representation of matrices e.g. $\boldsymbol{M}$
- Lowercase subscripts describe to which part a quantity belongs e.g. $\boldsymbol{f}_{\mathrm{i}}$, the i-th propeller force.
- $\mathbf{e}_{\mathrm{x}}$ describes the unit vector of the x-th dimension.
- Rotation matrices are indicated as follows: ${}^{\mathrm{B}}\mathbf{R}_{\mathrm{A}} \in \mathrm{SO}(3)$ is defined as the rotation matrix of the rotation from coordinate frame A to coordinate frame B.
- ${}^{\mathrm{B}}\mathbf{p}_{\mathrm{A}} \in \mathbb{R}^3$ is the translation vector from A to B.
- $\boldsymbol{R}$ is the rotation matrix from the body frame to the world frame ${}^{W}\boldsymbol{R}_{B}$.
- $\boldsymbol{p}$ is the translation vector from the body frame to the world frame ${}^{W}\boldsymbol{p}_{B}$.
- $\boldsymbol{a}^{\top}$ indicates the transpose of $\boldsymbol{a}$.
- $\boldsymbol{A}^{-1}$ indicates the inverse of $\boldsymbol{A}$.
- $\boldsymbol{J}_{>0} \in \mathbb{R}^{3\times3}$ represents the inertia matrix
- $m_{>0} \in \mathbb{R}$ represents the total mass of the drone
- $\boldsymbol{O}_{A\times B}$ is the zero matrix of size A by B.
- $\boldsymbol{I}_{A\times B}$ is the identity matrix of size A by B.
- ${}^{B}Ad_{A} \in \mathbb{R}_{6\times6}$ is the adjoint of the transformation from A to B.
- α is the tilt angle of the rotors of the OmniMorph.

2.1.1 Coordinate frames

To properly describe the OmniMorph and the sensor used, several coordinate frames are used:

- $\mathscr{F}_{\mathrm{W}} : \{\mathscr{O}_{\mathrm{W}}, \boldsymbol{x}_{\mathrm{W}}, \boldsymbol{y}_{\mathrm{W}}, \boldsymbol{z}_{\mathrm{W}}\}$ which is defined as the inertial world fixed frame. For simplicity, the inertial world fixed frame is the standard frame used when the relative frame is not explicitly described.
- $\mathscr{F}_{\mathrm{B}} : \{\mathscr{O}_{\mathrm{B}}, \boldsymbol{x}_{\mathrm{B}}, \boldsymbol{y}_{\mathrm{B}}, \boldsymbol{z}_{\mathrm{B}}\}$ which is defined as the body frame located at the center of mass (CoM) of the UAV.
- $\mathscr{F}_{P_i} : \{\mathscr{O}_{P_i}, \boldsymbol{x}_{P_i}, \boldsymbol{y}_{P_i}, \boldsymbol{z}_{P_i}\}$ corresponding to the frame of the i-th rotor located at the center of the propeller. This frame is attached to the motor's stator, meaning it does not rotate with the propeller. With this representation, the thrust generated by the propeller will always be along $\boldsymbol{z}_{P_i}$.
- $\mathscr{F}_{\mathrm{S}} : \{\mathscr{O}_{\mathrm{S}}, \boldsymbol{x}_{\mathrm{S}}, \boldsymbol{y}_{\mathrm{S}}, \boldsymbol{z}_{\mathrm{S}}\}$ is the sensor frame of the force torque sensor located at the center of the area of contact of the sensor to the attachment which is measured.

The $\mathscr{F}_{\mathrm{P}_i}$ are all translationally attached to the $\mathscr{F}_{\mathrm{B}}$ making the translation from the propeller to the body ${}^{\mathrm{B}}\mathbf{p}_i$ for each of the propellers constant. Note that, due to the tilting of the propellers, ${}^{\mathrm{B}}\mathbf{R}_{\mathrm{P}_i}$ is not constant. A representation of these frames can be seen in Figure 2.2. Figure 2.1 shows how the body frame relates to the different propellers with tilt angle α.

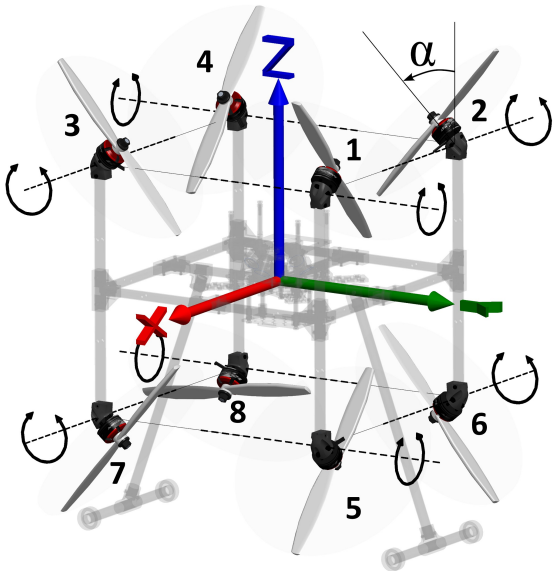

Figure 2.1: Representation of the OmniMorph with body frame $\mathcal{F}_B$ and the tilt angle α of the rotors. Credit:Aboudorra et al. (2024).

2.2 Modeling

This section will start with the standard modeling of the forces and moments present due to spinning propellers. These forces are then translated to the center of mass and will influence the total dynamics of the UAV. Some explanation is given about different degrees of actuation for the OmniMorph and the equation to calculate the power on a rotor is shown.

2.2.1 Propeller Forces and Moments

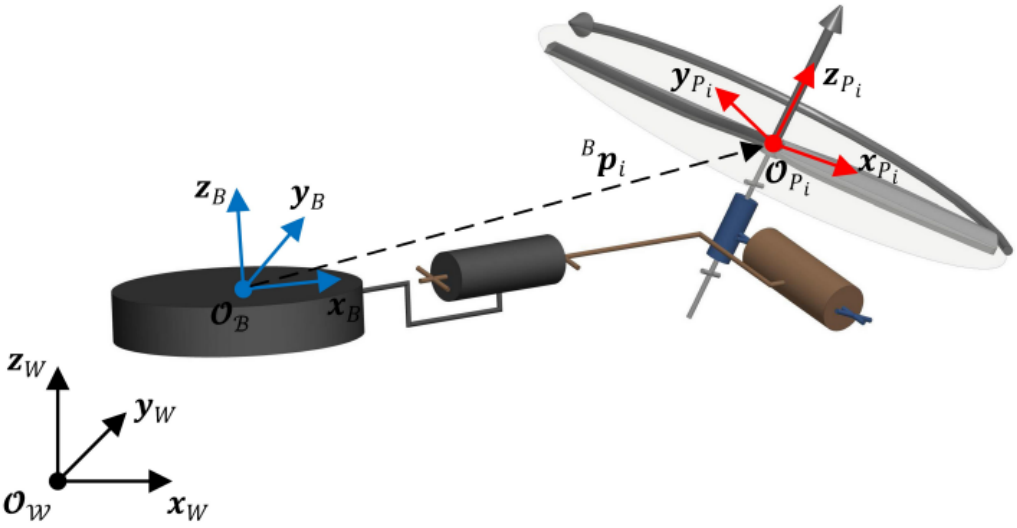

Figure 2.2: Visual representation of the propeller attached to the body. Note the different coordinate frames and the translation between the propeller and body frame. Credit: Franchi (2023).

In Figure 2.2, the propeller frame $\mathcal{F}_{P_i}$ and body frame $\mathcal{F}_{P_i}$ can be seen. The each of the propeller frames has been defined in such a way that the thrust force and drag moment of the

propeller is always applied along the z-axis. This means the propellers apply no thrust in either the $\boldsymbol{x}_{P_i}$ and $\boldsymbol{y}_{P_i}$ components. Note that, depending on the chord configuration of the propeller, these can be in the same direction or in opposite directions. To derive an expression for the magnitude of the force and moment produced, the angular velocity of the propeller is defined as $\bar{\omega}_i$ and is positive when it has the same direction as $\boldsymbol{z}_{P_i}$.

The propeller rotating through the air produces the drag moment and is always in the opposite direction of $\bar{\omega_i}$. Its norm is proportional to the square of the norm of the angular velocity $\bar{\omega_i^2}$ Franchi (2023). The drag moment possesses a constant coefficient c_τ that encompasses a combination of aerodynamic properties of the propeller and the fluid it spins in, such as the propeller shape, its spatial distribution, the air density, etc. We define k_i to be the chord configuration of the propeller. There are two possible configurations depending on whether the blades of the propellers are pitched downwards or upwards, looking from the centre of the propeller. These are called descending and ascending chord propellers. k_i is either 1 (descending) if a positive direction of the angular velocity produces a force in the positive $\boldsymbol{z}_{P_i}$. Otherwise, it is -1 (ascending), and a negative angular velocity direction will produce a positive force in the $\boldsymbol{z}_{P_i}$. The chord of the propeller can be modelled in either the moment or the force equation. The choice is made to include the chord of the propeller in the moment equation. To do this, the rotor's angular velocity is substituted with $\omega_i = k_i\bar{\omega}_i$. All the variables discussed above combine into the following equation for the drag moment $\boldsymbol{m} \in \mathbb{R}^3$:

$$\boldsymbol{m}_{P_i} = -k_i c_\tau |\omega_i|\omega_i \boldsymbol{z}_{P_i} \tag{2.1}$$

Similarly to the moment, the force produced by the propeller is also proportional to the square of the norm of the angular velocity ω_i^2. It is modelled with a constant coefficient c_f whose value depends on how much lift the propeller can produce. This means that the force that a propeller produces, $\boldsymbol{f} \in \mathbb{R}^3$, can be modeled through the following equation:

$$\boldsymbol{f}_{P_i} = c_f |\omega_i|\omega_i \boldsymbol{z}_{P_i} \tag{2.2}$$

The motors that we are using are controlled through electronic speed controllers (ESCs). This means that the angular velocity of each of the propellers can be controlled. The square of the angular velocity can be defined as the input $|\omega_i|\omega_i = u_{\lambda i} \in \mathbb{R}$. The output force and moment of the propeller, depending on the new input, become:

$$\boldsymbol{f}_{P_i} = c_f u_{\lambda i} \boldsymbol{z}_{P_i} \tag{2.3}$$

$$\boldsymbol{m}_{P_i} = -k_i c_\tau u_{\lambda i} \boldsymbol{z}_{P_i} \tag{2.4}$$

2.2.2 Forces and Moments in body frame

Now that the model for a single propeller has been derived, we need to understand how these affect the total force and moment of the drone. This implies that we look at the forces and moments exerted by the propellers w.r.t. the body frame $\mathscr{F}_\mathrm{B}$. These equations can be seen in Equation 2.5 and 2.6. Note that, in Equation 2.6, the total moment is an addition of 2 components. The first component is the moment produced on the body due to the propeller drag. The second component is due to the moment produced as a result of the force being applied at a distance ${}^B p_i$ from $\mathscr{F}_\mathrm{B}$.

$$\boldsymbol{f}_i^B = (c_f \boldsymbol{z}_{P_i}) u_{\lambda i} \tag{2.5}$$

$$\boldsymbol{m}_i^B = (-k_i c_\tau \boldsymbol{z}_{P_i} + c_f {}^B\boldsymbol{p}_i \times \boldsymbol{z}_{P_i}) u_{\lambda i} \tag{2.6}$$

The vector consisting of the forces and moments in a frame is called the wrench $\boldsymbol{w} \in \mathbb{R}^6$. With the Equations 2.5 and 2.6, we can calculate the wrench in $\mathscr{F}_\mathrm{B}$ due to a propeller thrust. In this

thesis, a force torque sensor was used to directly measure the wrench output from a propeller in the sensor frame $\mathscr{F}_S$. Using Chapter 2 of Sastry (2017), we can transform the effect of a wrench in $\mathscr{F}_S$ to $\mathscr{F}_B$ with Equation 2.7.

$$\boldsymbol{w}^B = {}^S Ad_B^\top \boldsymbol{w}^S \tag{2.7}$$

Writing out the adjoint ${}^S Ad_B^\top$, the final equation for the wrench transformation in Equation 2.8 can be used.

$$\begin{bmatrix} \boldsymbol{f}_i^B \\ \boldsymbol{m}_i^B \end{bmatrix} = \begin{bmatrix} {}^B\boldsymbol{R}_S^\top & \boldsymbol{O}_{3\times3} \\ -{}^B\boldsymbol{R}_S^\top {}^B\boldsymbol{p}_S\times & {}^B\boldsymbol{R}_S^\top \end{bmatrix} \begin{bmatrix} \boldsymbol{f}_i^S \\ \boldsymbol{m}_i^S \end{bmatrix} \tag{2.8}$$

2.2.3 Dynamics of the OmniMorph

Previously, we defined $u_{\lambda i}$ as input for each of the eight propellers. For the OmniMorph it is not only possible to control each of the propeller velocities but also the tilt angle alpha (α) of the propellers with a single servo motor. Therefore, the total inputs of the system are $\boldsymbol{u} = [\ \boldsymbol{u}_\lambda^\top\ \alpha\ ]^\top \in \mathbb{R}^9$. The total wrench on the body due to the thrust of the propellers can be computed by summing the forces and moments each of the propellers has on the body. This can be seen in Equation 2.9.
The actuation wrench can then be rewritten in the form of Equation 2.10 where $\boldsymbol{A}(\alpha)$ represents the angle-dependent allocation matrix. This form relates the input throttle to the actuation wrench of the platform depending on the tilt angle α.

$$\boldsymbol{w}(\boldsymbol{u}) = \begin{bmatrix} \boldsymbol{f}_B^B(\boldsymbol{u}) \\ \boldsymbol{m}_B^B(\boldsymbol{u}) \end{bmatrix} = \sum_{i=1}^{8} \begin{bmatrix} \boldsymbol{f}_i^B(\boldsymbol{u}) \\ \boldsymbol{m}_i^B(\boldsymbol{u}) \end{bmatrix} \tag{2.9}$$

$$\boldsymbol{w}(\boldsymbol{u}) = \boldsymbol{A}(\alpha)\boldsymbol{u}_\lambda \tag{2.10}$$

The actuation wrench has an effect on the standard dynamic equations for the drone. From Hamandi et al. (2021), the dynamic equations for an actuated rigid body following Newton-Euler formalism are as follows:

$$\begin{bmatrix} m\ddot{\boldsymbol{p}}_B \\ \boldsymbol{J}_B\dot{\boldsymbol{\omega}}_B \end{bmatrix} = -\begin{bmatrix} mgz_W \\ \omega_B \times \boldsymbol{J}_B\omega_B \end{bmatrix} + \boldsymbol{G}\boldsymbol{w}(\boldsymbol{u}) \tag{2.11}$$

Where m is the mass of the drone, $\boldsymbol{J} \in \mathbb{R}^{3\times3}$ and $\boldsymbol{G}$ represents the transformation matrix:

$$\boldsymbol{G} = \begin{bmatrix} \boldsymbol{R}_B & \boldsymbol{O}_{3\times3} \\ \boldsymbol{O}_{3\times3} & \boldsymbol{I}_{3\times3} \end{bmatrix} \tag{2.12}$$

2.2.4 Actuation

To see the effect of minor deviations in input on the wrench, the full allocation matrix $\boldsymbol{F}(\boldsymbol{u}) \in \mathbb{R}^{6\times9}$ is introduced in Equation 2.13. $\boldsymbol{F}_1(\alpha) \in \mathbb{R}^{6\times8}$ constitutes the effect that a variation of the thrust has on the wrench while $\boldsymbol{F}_2(\boldsymbol{u}_\lambda, \alpha) \in \mathbb{R}^6$ constitutes the effect of a change in tilt angle on the wrench. The full allocation matrix can be seen in Appendix A where c_α is the cosine of α, s_α is the sine of α and L is the side length from the body to the rotor along the $\mathscr{F}_B$ axis Aboudorra et al. (2024).

$$\boldsymbol{F}(\boldsymbol{u}) = \frac{\partial \boldsymbol{w}}{\partial \boldsymbol{u}} = \begin{bmatrix} \frac{\partial \boldsymbol{f}}{\partial \boldsymbol{u}_\lambda} & \frac{\partial \boldsymbol{f}}{\partial \alpha} \\ \frac{\partial \boldsymbol{m}}{\partial \boldsymbol{u}_\lambda} & \frac{\partial \boldsymbol{m}}{\partial \alpha} \end{bmatrix} = \begin{bmatrix} \boldsymbol{F}_1(\alpha) & \boldsymbol{F}_2(\boldsymbol{u}_\lambda, \alpha) \end{bmatrix} \tag{2.13}$$

The allocation matrix is an essential part of determining the degree of actuation of drones. Figure 2.4 shows the relation between the different degrees of actuation. Note that the rank of the

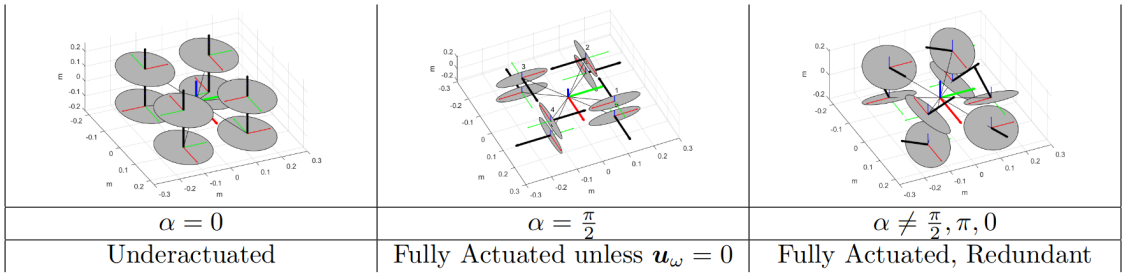

$\alpha = 0$	$\alpha = \frac{\pi}{2}$	$\alpha \neq \frac{\pi}{2}, \pi, 0$
Underactuated	Fully Actuated unless $\boldsymbol{u}_\omega = 0$	Fully Actuated, Redundant

Figure 2.3: Figure showing the degree of actuation for the different α of the OmniMorph. Credit: Aboudorra et al. (2023).

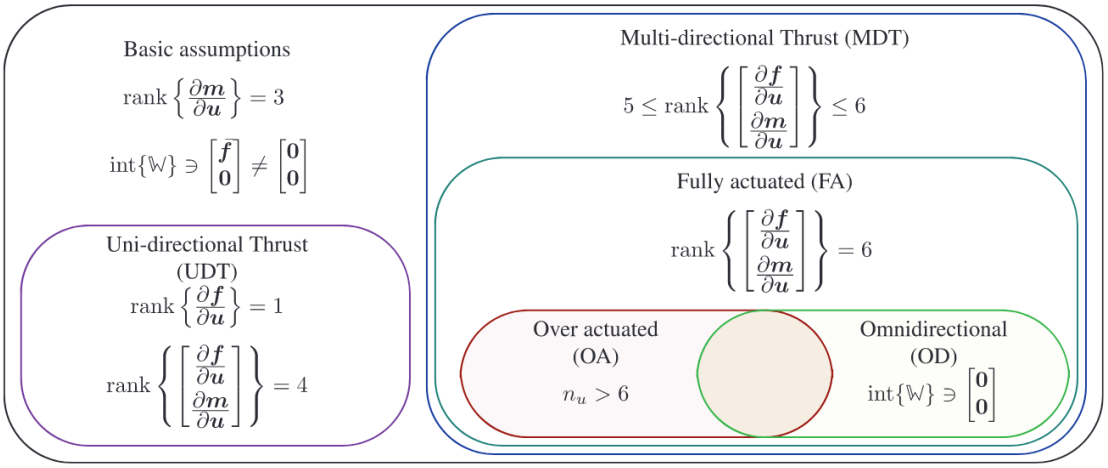

Figure 2.4: interaction between thrust-related properties for multirotor designs. Credit: Hamandi et al. (2021) ©SAGE Publications.

allocation matrix is what determines the degree of actuation, and some additional conditions can make the platform omnidirectional. For the OmniMorph, the degree of actuation of the platform varies through the change in α. From the table in Figure 2.3, we can distinguish three different degrees of actuation. In the first case, the platform is underactuated (UA). Due to its rotors all pointing in the z-direction, it is unable to produce a force in either the x-direction or the y-direction without changing its orientation. It is possible to determine if the platform is underactuated (UA), Fully actuated (FA), or Omnidirectional (OD) by looking at the rank($\boldsymbol{F}(\boldsymbol{u})$). An underactuated platform means that the UAV cannot independently create a thrust or a moment in a direction. An example of this is the standard quadrotor. It is able to produce a thrust along the z-direction. However, it is unable to produce a force along the x or y direction without tilting. The force in x and y is thus coupled to the moment around x and y.
A fully actuated platform is able to produce a force and a moment in any direction independently. For a platform to be fully actuated, the rank($\boldsymbol{F}(\boldsymbol{u})$) must be 6.
In the case of $\alpha = 0$, the rank($\boldsymbol{F}_1(\alpha)$) = 4 so the platform is UA. When $\alpha = \frac{\pi}{2}$, the rank($\boldsymbol{F}_1(\alpha)$) = 5 meaning it produces multi-directional thrust. As shown in Figure 2.3, the platform can produce thrust along the x and y-axis but not along the z-axis. As we are designing an omnidirectional platform, it is more interesting to see that, when $\alpha \neq 0, \frac{\pi}{2}, \pi$ the rank($\boldsymbol{F}_1(\alpha)$) = 6. For OD, the OmniMorph needs to satisfy an additional condition. Namely, it needs to be able to hold its weight in every pose. A more concrete way of saying this is that the set of feasible forces for a value of α must envelop the full sphere representing the gravitational force, which has a radius mg. This has previously been determined to be from $\alpha \approx$37 degrees Aboudorra et al. (2024).

2.2.5 Power

Previously, the equations have been derived for the force and the moment of the rotor. Another important aspect to consider is the power draw of each of the rotors, as we will look into the efficiency of the OmniMorph at different values of α. The power necessary to fly a drone is an important aspect of the design of a drone. This is due to the compromise that has to be done between the weight and capacity of the batteries Delbecq et al. (2020). A heavier battery will result in a bigger battery capacity but more weight. This means the platform has to constantly exert more power to hover, which decreases its flight time. For the OmniMorph, the morphing ability is used to fly in the most energy-efficient configuration.

The power can be computed in two different ways. The first option is to look at the electrical power. This can be computed through Equation 2.14 where U is the voltage and I the current. The current consumption data of each of the rotors is saved, and the input voltage of the OmniMorph was set at 16 V. As the tests have been done on a stationary setup, a power supply was used for convenience and safety reasons.

$$P = UI \tag{2.14}$$

Unfortunately, during the experiments, the voltage on the power supply was constant, but the voltage was not continuously monitored through the software. When the voltage was measured through software commands, the actual voltage measured changed throughout the experiment. This made retrieving the power through Equation 2.14 unreliable. A second method of retrieving the power is by computing the mechanical power. From rotational kinematics, Equation 2.15 represents the mechanical power. Note that, ω is in rad/s and τ is the total moment in Nm. The mechanical power is not the same as the total power. Power loss due to heat and the power required by components other than the rotors is not taken into account when calculating the mechanical power. As we are interested in the difference in power for different moments due to changes in aerodynamic interference, it is possible to calculate this effect with the mechanical power of Equation 2.15.

$$P = \tau\omega \tag{2.15}$$

3 Aerodynamics of the OmniMorph

In Section 2.2, we have seen that the aerodynamics of a drone according to the standard models are modelled by the constant coefficients c_τ and c_f. However, these coefficients are only an approximation of the real effects of aerodynamics. In this section, a deeper look will be taken into the underlying aerodynamics of the OmniMorph.

3.1 General aerodynamic effects

c_τ and c_f are both parameters resulting from the interaction of the propellers with the air. Mahony et al. (2012) define the aerodynamic effects of c_f as a combination of C_T, the thrust coefficient depending on the rotor geometry and profile, ρ, the density of air, A, the area of the rotor and r^2, the radius squared. c_τ is said to also depend on these except for C_T. Even this is an approximation to the real effect. Chapter 2 of Leishman (2016) goes into much further detail by estimating non-ideal effects such as induced tip loss and the blade loading coefficient. As we are fundamentally looking into the simplest model which results in the best performance, these effects are left out.

Aerodynamic effects due to the environment can also influence the drone. These effects include wind, moisture, and obstruction of airflow due to the proximity of walls, ceilings, or other objects that restrict airflow. As all tests done during this thesis have been done in a flight lab, these effects are neglected.

Next to this, secondary aerodynamic effects take place, which are usually also neglected in UAV models. The most fundamental additional secondary aerodynamic effects are blade flapping and induced drag Mahony et al. (2012).

3.1.1 Blade flapping and induced drag

The propellers on UAVs are usually very lightweight and have some flexibility to them. When the propeller is spinning, it experiences a variety of aerodynamic and inertial forces, which will flex the propeller to various degrees. A small amount of flex is usually necessary to prevent the transmission of aerodynamic forces to the rotor hub, which can break as a result of this Mahony et al. (2012).
Induced drag is an effect that occurs mainly due to the rigidity of the rotor instead of the flexibility of the rotor. These effects occur during lateral translations through the air. As the tests done during this thesis have been done on a stationary platform, these are not relevant for this thesis but should be taken into account when the platform will fly.

3.2 Additional effects for the OmniMorph

Due to the rotor configuration of the OmniMorph, the bottom layer of rotors lies directly underneath the top rotors. When the top rotor spins, it will speed up the air. The accelerated airflow will reach the propeller underneath and will potentially have more difficulty producing thrust. Hamandi et al. (2020) mentioned the effect of the propeller airflow cylinder intersection in their design as one of the drawbacks. In the case of the OmniMorph, the cylinders projected by the area of the rotors spinning are on top of each other when $\alpha = 0$. The more the propellers tilt, the more the cylinders are projected away from the other rotors.
In general UAV platforms, the effect of the rotors on each other is not modelled. It is possible that this effect is present for some platforms. For the OmniMorph, it has been seen that this

effect is significantly present. Experiments have been designed to bring into view the effects of aerodynamic interference for a new model to be proposed. This model is more complex than the standard model but still as simple as possible. The focus of the analysis was on the OmniMorph, but this thesis gives insights into some effects which could be used in a more general way for some platforms. One of the options is to regard c_f and c_τ as variables instead of constants. These can be varied per rotor for different tilt angles and the amount of aerodynamic interference the rotor is subjected to.

4 Omnimorph Prototype

This chapter will discuss the hardware and software of the OmniMorph prototype. The prototype used for this thesis has been used previously for testing flight in the underactuated (UA) configuration. The platform lacks the servo mechanism that will be in the final prototype of the OmniMorph. During this thesis, a clone of this platform was created. This version was not used but could, in the future, serve to test the tilting mechanism. Figure 4.1a shows a CAD model representation of the platform. Figure 4.1b shows a picture of the physical prototype.

4.1 Hardware

This section will show the different components used and the constants that are important for the OmniMorph. The prototype used did not possess the tilt mechanism yet. This means the rotors cannot actively tilt, making all the joints static. However, the rotors of the prototype can be tilted at different angles by swapping 3D-printed components, which are printed to simulate the tilt mechanism at a set tilt angle. As shown in Figure 2.3, some of the tilt angles would theoretically enable the prototype to hover in all orientations, making the platform omnidirectional (OD). The specifications of the drone are listed in Table 4.1.

4.1.1 Components

The components used for this platform are listed below. Appendix B shows how the OmniMorph is connected. The real platform will have a battery, and this is taken into account in the total mass, however, as the platform was stationary for testing, a power supply was used.

Single board computer

The single board computer used for this platform is an Odroid XU4 [1]. It is running Ubuntu 20.04 for Odroid. The Odroid is the higher level controller, which is in charge of the communication to the PC, relaying input information to the flight controller, saving data, and could, in the future, be used for implementing more complex control algorithms.

Flight controller

The flight controller used for the prototype is the Paparazzi Chimera V1.00 [2]. The flight controller sends the desired velocity back to the ESCs. The flight controller is also in charge of gathering data from the ESCs and communicating important information back to the Odroid.

[1] https://wiki.odroid.com/odroid-xu4/odroid-xu4
[2] https://wiki.paparazziuav.org/wiki/Chimera/v1.00

Symbol	Value	Definition
m	1.25 Kg	Mass of the platform
D	25 cm	Distance between the propellers
α_{min}	0 degrees	Minimum tilt angle of the platform
α_{max}	50 degrees	Maximum tilt angle of the platform

Table 4.1: Specifications of the drone.

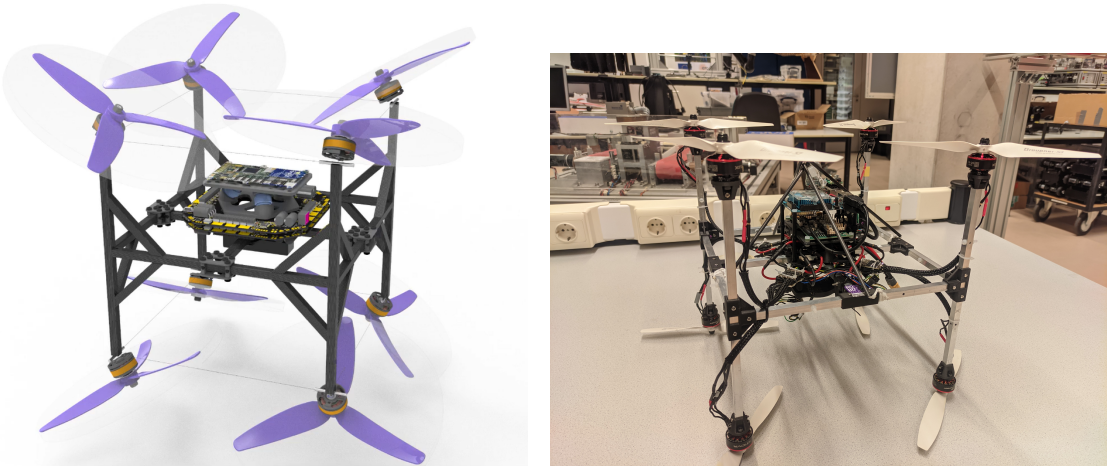

(a) CAD model of the OmniMorph.

(b) Picture of the OmniMorph prototype.

Figure 4.1: A comparison between the prototype of the OmniMorph and a CAD model of the OmniMorph.

Electronic Speed Controllers (ESCs)

The ECSs used for this thesis are the Kiss Racing 32A ESCs [3]. The ESCs receive control inputs from the flight controller and translates this to three-phase current outputs that go to the motors. As the platform is an octo-rotor, 8 ESCs were used.

Motors

The eight motors used are the Xnova Lightning V2 2208-2500 [4] which is the 2500KV version of the Xnova motors.

Propellers

The eight propellers used are the Graupner 3Dprop 8x4.5 bidirectional nylon propellers. They have two blades.

Platform

The frame consists of square aluminium hollow bars with 3D-printed corners. The platform has multiple layers in its center, which houses the Odroid on top, the Paparazzi in the middle, the power distributor below that, and the battery at the bottom.

4.2 Software

The main PC runs Ubuntu 20.04. The user interface consists of a combination of Matlab and Simulink. The architecture used to communicate and connect to the UAV is the Genom3 architecture suite from Openrobots Mallet et al. (2023) developed at LAAS CNRS [5]. It uses a publisher/subscriber architecture similar to ROS and is a modular component-based software suite. Through the use of various Genom components, Matlab can be connected to the UAV. With the Simulink components of Genom, data can be monitored, and data can be sent to the instance of Genom running on the UAV. A schematic representation of way the software interacts with its main components can be seen in Appendix C.

[3] https://www.flyduino.net/en_US/shop/product/pr2200kissesc36s32a45alimit32bitbrushlessmotorctrl-2961?category=2

[4] https://www.xnovamotors.biz/category-4/xnova-lightning-v2-2208-2500kv-set.html?language=en

[5] https://www.laas.fr/en/

5 Experiments

A multitude of different experiments have been performed to answer the research questions. This chapter will first introduce the different setups used for the experiments and then explain the process and results of each of the experiments performed. The experiments will first determine the hovering velocity. When the hovering propeller velocity has been established, the corresponding c_τ and c_f are established. Then, the effects of aerodynamic interference are estimated. After this, different solutions to minimize the aerodynamic interference are discussed.

5.1 Experiment setup

Two different setups were created to find the answers to the research questions. These two have been represented in Figure 5.1.
The first setup consists of fixing the OmniMorph on a force torque sensor. This enables us to measure the total forces and torques on the CoM resulting from the forces and torques applied by the rotors.
The second setup consists of separating one of the bottom motors from the OmniMorph. The OmniMorph is fixed on a beam and cannot move. The separated motor is fixed on a force torque sensor in the same location it would be if it was fixed to the OmniMorph. This setup is used to measure the aerodynamic effects on a single rotor. As the current prototype does not yet possess the mechanism to change α during operation, different brackets were 3D-printed at different fixed angles, which could be attached to the force torque sensor.
For both of the experiments, the ATI Mini 40 force torque sensor [1] was used to measure the force and torque in 6 degrees of freedom (Force and torque along the x-,y- and z-axis of the sensor).

All the experiments have been performed in a flight lab with the UAV at a similar location in the room. The experiments were done in similar climate conditions as to minimize the difference in results. As the UAV was stationary during operation, it was powered using a power supply. An emergency stop button was added between the power supply and the drone for additional safety and convenience.

[1] https://www.ati-ia.com/products/ft/ft_models.aspx?id=mini40

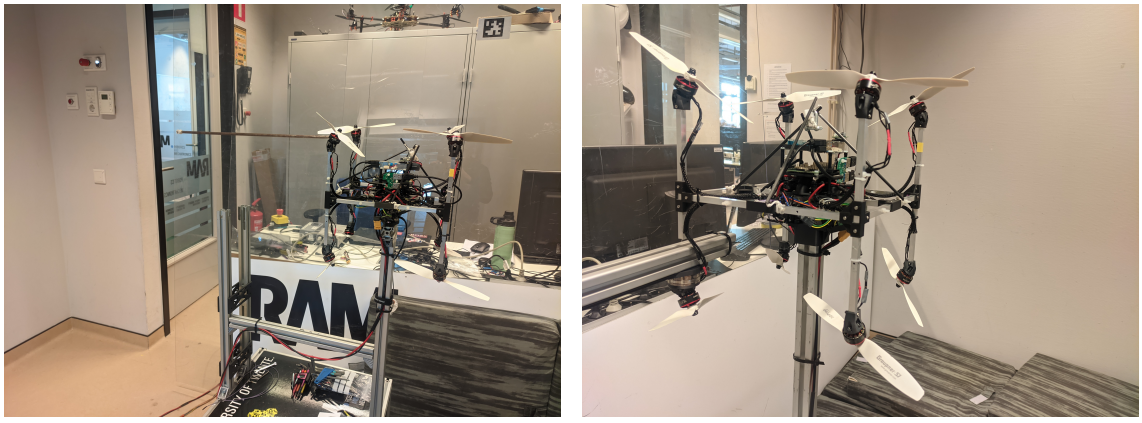

(a) Picture of the setup with the Omnimorph on the force torque sensor.

(b) Picture of the setup where a single rotor is attached to the force torque sensor.

Figure 5.1: Pictures of the different setups of the experiments performed on the OmniMorph.

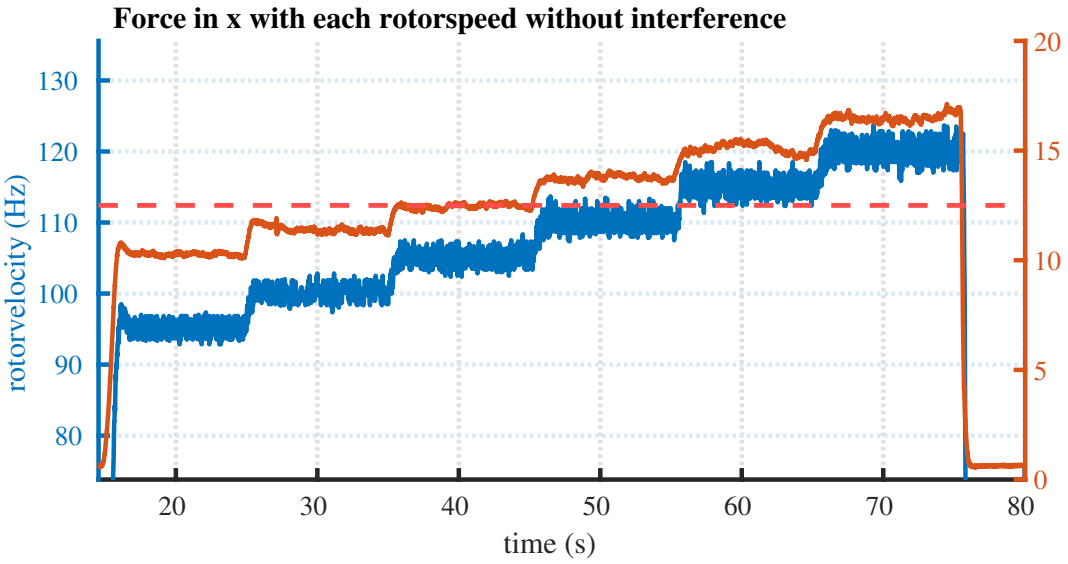

Figure 5.2: Figure stepping through the rotor velocities (blue) from 95 Hz to 120 Hz with 5 Hz increments over time with the associated the force in the z-direction (orange) on the full OmniMorph platform. Note the line corresponding to the force required for hovering at 12.5 N.

5.2 Hovering rotor velocity

The first experiment to be performed is to see whether the OmniMorph is able to sustain its own weight when all the propellers are in the most energy-efficient configuration, according to the simulations. This is at an α of 0 degrees. From this, the hovering speed of each of the propellers can be determined. The platform will not be able to fly if it cannot sustain its own weight. We have seen previously that the total weight of the platform is 1.25 kg. This means that the platform needs to output at least 12.5 N of force in the z-direction. Using the first setup, the velocity of the propellers was increased in a stepwise fashion with 5 Hz steps from 95 Hz until 120 Hz. This is plotted in Figure 5.2. From this, it was determined that the hovering propeller velocity is 105 Hz. This can be seen from the dotted line crossing the force at the time that the rotor velocity was 105 Hz.

5.3 Coefficient of drag and coefficient of force

As seen from Equation 2.3 and Equation 2.4, in the standard UAV model, c_f and c_τ are regarded as constants. However, in Chapter 3, it was mentioned that c_f and c_τ are dependent on different propeller parameters and aerodynamic effects. This experiment will focus on measuring c_f and c_τ without any aerodynamic interference of other rotors in order to quantify c_f and c_τ for the specific rotors of the OmniMorph and measure the effect of the propeller speed on c_f and c_τ.

The second experiment setup is used with the propeller at a 0 degree α. The forces and torques generated by the propeller will be directly transmitted to the force torque sensor. The propeller speed is increased stepwise every 10 seconds by 20 Hz from 20 Hz to 200 Hz. The results from this can be seen in Figure 5.3. From Equation 2.3 and Equation 2.4 can be seen that the force and torque of a rotor produced are dependent on the square of the velocity scaled by c_f and c_τ respectively. In Figure 5.4a, the force divided by the velocity squared has been plotted over time. In Figure 5.4b, the moment divided by the velocity squared has been plotted over time. From both Figure 5.4a and Figure 5.4b it can be seen that the c_f and c_τ are affected by different propeller velocities. This is expected as in Section 3, we have seen that the propellers are

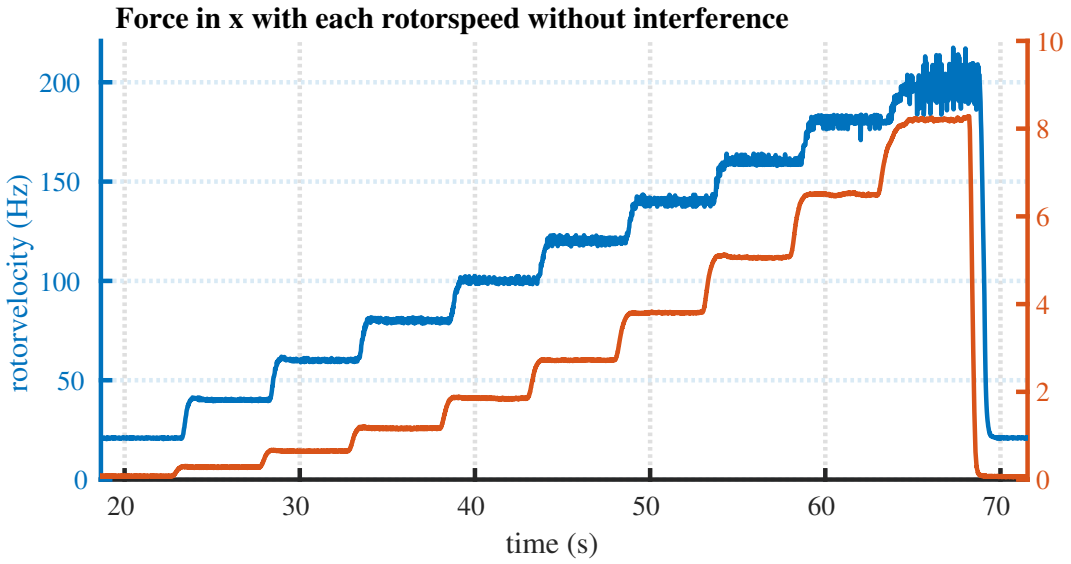

Figure 5.3: Figure showing the force in the z-direction (orange) associated with the rotor velocity (blue) increasing from 20 Hz to 200 Hz with 20 Hz step increments on a single motor. Note that a rotor velocity of 100 Hz is associated with a force of 1.75 N.

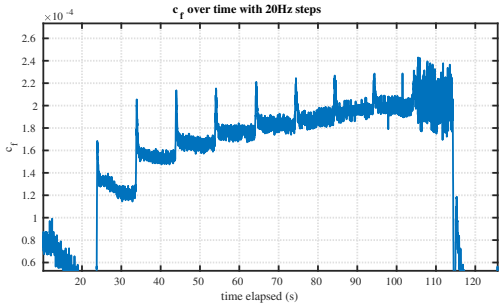

(a) Figure showing how the coefficient of force is changing with increasing rotor velocities.

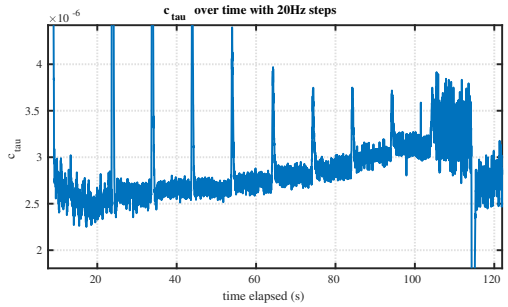

(b) Figure showing how the coefficient of torque is changing with increasing rotor velocities.

Figure 5.4: Coefficient of force and coefficient of torque measured at different rotor velocities.

designed to have a small amount of flex. This changes the properties mentioned that c_f and c_τ are dependent on.

To create a model that resembles reality as closely as possible, we choose the c_f and c close to the hovering speed. This is because most actions done with the Omnimorph will be around hovering. This results in a base c_f and c_τ of $2.8e^{-4}$ and $1.8e^{-6}$ respectively.

Another interesting point to note is that, when comparing the force output per propeller velocity in Figure 5.2 and the force per propeller velocity in Figure 5.3, it can be seen that the force output by the whole platform is not equal to eight times the force output by a single propeller. In the case of hovering, the force per propeller necessary for hovering is 1.57 N, equating to 12.5 N for the full platform. For the full platform, the hovering force was achieved at a propeller speed of 105 Hz, but looking at Figure 5.3, a single propeller speed of 100 Hz already corresponds to an output of 1.75 N. This means that the necessary hovering speed for a single propeller is lower than 100 Hz while for the full platform it is at 105 Hz.

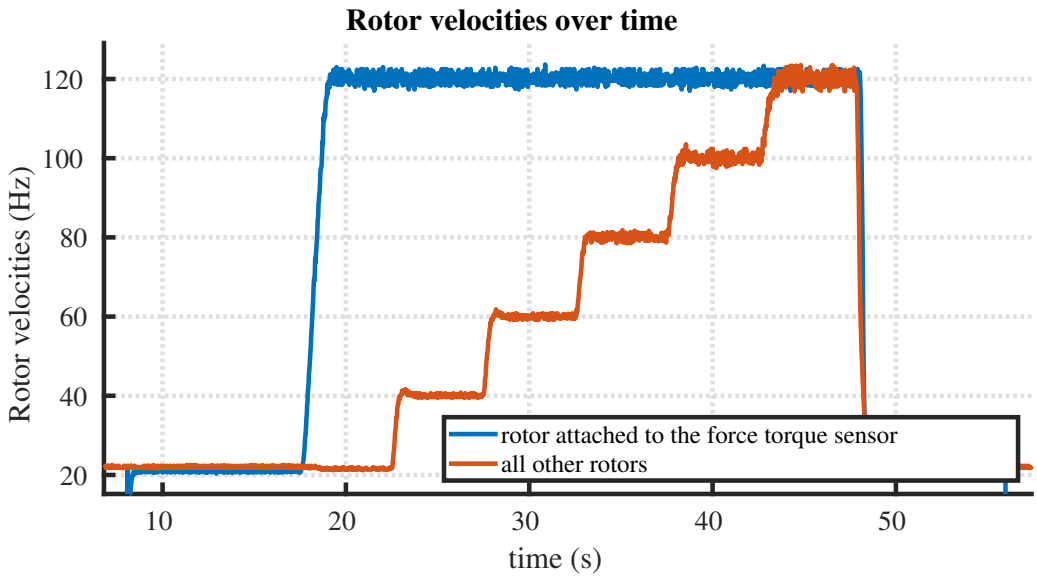

Figure 5.5: Rotor velocities over time. The rotor attached to the force torque sensor (blue) is at a fixed velocity of 120 Hz while the other rotors (orange) are stepping from 20 Hz to 120 Hz.

In order to account for this difference, a look will be taken at the effect that the aerodynamics of propellers have on each other. The hypothesis is that, in the configuration of the OmniMorph with α at zero, one rotor is directly above the other rotor, resulting in the top rotor creating airflow to the bottom rotor. The supposition is that this is what causes the bottom propeller to exert less force than predicted. The next section will take a deeper look into this effect.

5.4 Effects of aerodynamic interference

A multitude of experiments were performed in order to bring into view the true effects of aerodynamic interference on the rotors.

5.4.1 Effect on the bottom rotors

In order to quantify the amount of aerodynamic interference that the rotors experience, the second setup is used. We first investigate whether the bottom propeller loses force due to the other rotors spinning. This is done by starting with simply spinning the measured rotor without any interference at 120 Hz in order to establish a baseline of the force emitted by the rotor at a set velocity.
For the second part, the top rotor is increased with 20 Hz in a stepwise fashion while the same measured rotor underneath is spinning at 120 Hz. The velocities are shown in Figure 5.5. This enables us to see the force drop-off due to the other rotors. In Figure 5.6, it can be seen that the force exerted by the bottom rotor is dropping with each increase in the rotor velocity of the top rotor. Due to this effect, the full platform has to spin its rotors faster in order to compensate the force lost. When the platform is spinning all rotors at 120 Hz, the force lost in each of the bottom propellers is 0.92 N which is a decrease of 34 %.

5.4.2 Propeller with the most influence on the aerodynamic interference

The next experiment is done to investigate which rotors have the biggest effect on the aerodynamic interference of a single rotor. Again, the second setup is used, and the same baseline is used with the force output of a single rotor which is spinning at 120 Hz. Three different meas-

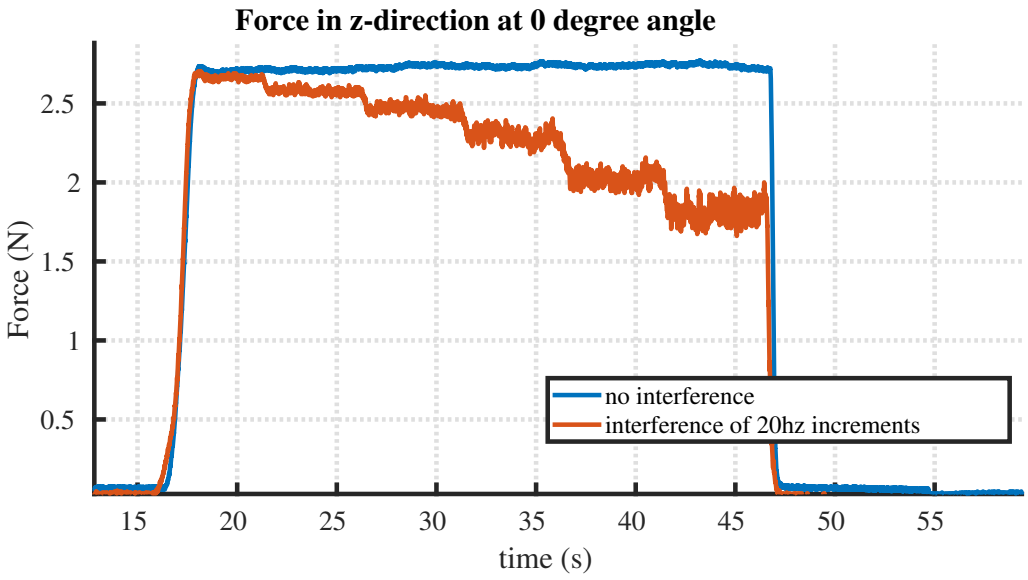

Figure 5.6: Figure showing the difference in output force comparing a rotor without aerodynamic interference (blue) to a rotor subject to aerodynamic interference from other rotors (orange).

urements were done to bring into view which rotor has the most effect on the aerodynamics. The first one is to spin all seven of the remaining propellers in the same stepwise fashion of 20 Hz. This is portrayed by the yellow line in Figure 5.7. The second part is to spin only the rotor directly above the rotor that is measured, which is the blue line in Figure 5.7. The last part is to spin all the rotors except the top rotor in a stepwise fashion. The effect of this on the measured rotor is portrayed by the purple line in Figure 5.7. What can be seen from this is that, at lower rotor velocities, the rotors other than the rotor directly above the measured rotor have some influence on the measured rotor but, as the velocity increases, the bulk of the aerodynamic interference is caused by the rotor situated directly above the measured one. This is interesting because in order to derive a model for the aerodynamic effects that is not overly complex, the model could only take the rotor directly above it into account.

5.4.3 Effect on the top rotors

It was just shown that aerodynamic effects from the top rotors influence the bottom rotors. However, we do not yet know what the effects of aerodynamic interference caused by the bottom rotor are on the top rotor. Intuitively, as the air is pushed down, the bottom and adjacent rotors should not interfere with the aerodynamics of one of the top rotors in any significant way. However, in order to be sure, this effect has been measured. As the experimental setup did not accommodate the measurement of the top rotors but only the bottom one, the bidirectional property of the propeller is used, and the thrust of the propellers is directed in the negative z-direction. This means the propellers apply a downward thrust, and the airflow is propelled upwards. We assume that the influence of gravity on airflow can be neglected within the distance of separation between the rotors, which is 25 cm.
First, the second setup is used with the propeller at 0 degree α to determine if the force exerted by the propeller is similar to positive and negative thrust. This would prove that the propeller is not only bidirectional but that the parameters of the propeller are similar regardless of the spinning direction. Figure 5.8 shows a comparison of the absolute value of the force when the propeller velocity is increased with steps of 20 Hz to 120 Hz against the same propeller when the propeller speed is decreased with steps of 20 Hz to -120 Hz. What can be seen is that the forces exerted by the propeller are similar, which proves that the propeller has similar

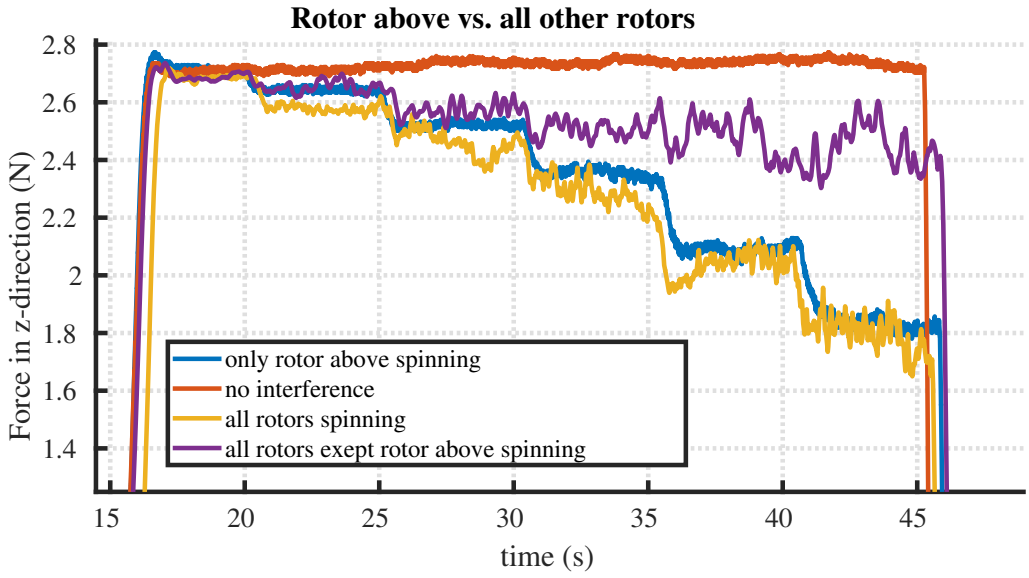

Figure 5.7: Figure showing the effects of interference of only the propeller above the measured propeller(blue), the effects without any interference (orange), all the propellers (yellow), and all the propellers spinning except the one above the measured propeller (purple).

behaviour regardless of the direction of the velocity.

With this knowledge and the assumption that the gravitational effect on air is neglected, both the top and bottom propellers can be thrust in the negative direction to simulate the effects of the bottom propeller on the top propeller. In Figure 5.9, the effect is investigated. A baseline is created by spinning the measured rotor at -120 Hz without any other propeller spinning. Then, the measured propeller is spun at -120 Hz while the top rotor is spun at stepwise intervals of -20 Hz down to -120 Hz. Additionally, a look is taken into the effect of the propellers spinning in opposite directions. The measured rotor is spun again at -120 Hz, and the top rotor is spun at stepwise intervals of 20 Hz up until 120 Hz. This situation will not frequently happen in a real flight scenario as the force in the z-axis of one propeller cancels out the force of the second one, making it a very energy-inefficient situation. This scenario has been investigated nonetheless for completion. The result of both these effects can be seen in Figure 5.9. From this figure it can be seen that there is no significant effect caused by the bottom rotor on the top rotor. This means that the rotors on top of the OmniMorph do not suffer from additional effects due to aerodynamic interference.

5.5 Accuracy of the wrench execution

The accuracy of the wrench execution is important to know because it quantifies how much the wrench with interference differs from the wrench without any aerodynamic interference. As seen in Chapter 2, the wrench is the 6-dimensional vector consisting of the forces and moments in 3-DoF on the body due to the thrust of the propellers. The force component of the wrench can be found by increasing the propeller velocity of the full platform. This will result in a force in the z-direction, which is most important for hovering accuracy. The accuracy of the moment is more complicated as the OmniMorph will have a moment of 0 in all directions while hovering. To find the accuracy of the moment execution, we translate the moment on a single propeller to the body.

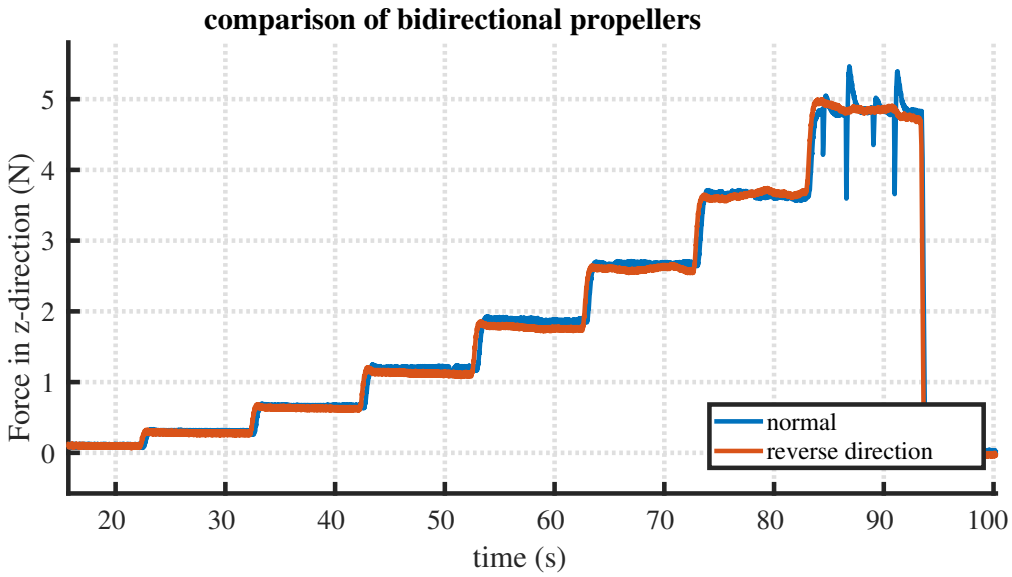

Figure 5.8: Figure showing that the force on the rotor is similar when spun in one direction against the same rotor spun in the other direction. The blue peaks are due to an ESC error failing to match the velocity and do not affect the final conclusion.

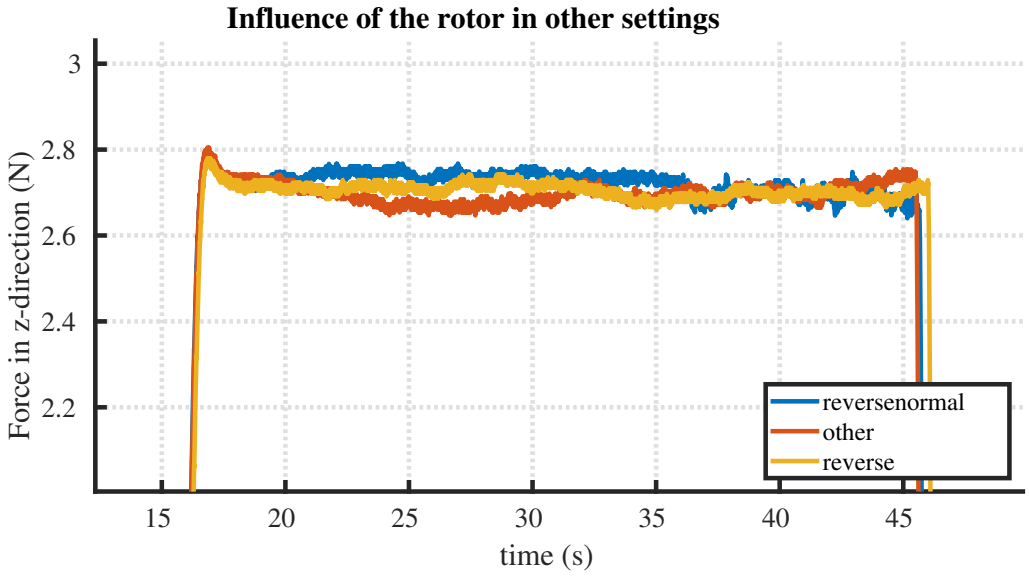

Figure 5.9: Figure showing the effects of different configurations of rotors on the top rotor. These are: When the propellers are opposed to each other (blue), when both propellers are spinning in the negative z-direction (orange) and when only the propeller attached to the force torque sensor is spinning in reverse.

5.5.1 Force components of the wrench execution of the CoM

By using the first experimental setup with the force torque sensor, the forces and moments on the body can be measured. c_f and c_τ have been determined by the previous experiments. We can use these to create the allocation matrix with these coefficients for different values of alpha. These allocation matrices can be used with different velocities to compute the wrench for the case in which there is no interference present. By comparing the wrench exerted by the allocation matrix and the wrench measured through the experiment, the accuracy of the wrench execution can be found, and the influence of the aerodynamic interference on the body can be determined. The bottom propellers will be subject to aerodynamic interference during the experiment, while the allocation matrix follows the standard model with a constant coefficient of force and torque.
The experiment performed is to increase the propeller velocities of all the rotors from 20 Hz to 120 Hz in a stepwise fashion with 20 Hz increments. Figure 5.10 shows the total force from the force torque sensor against the total force calculated through the allocation matrix for the angles of 0 degree, 10 degree, 30 degree and 50 degree α over time with this increase. As expected, the produced force output with interference is lower than the force output without interference. To find the accuracy, we plot the ratio between the force loss by interference and the measured force with interference. This has been plotted in Figure 5.11. It can be seen that this ratio corresponds to a different near-constant value for each angle. The choice was made to regard this ratio as a different constant for each angle. The reason behind this is that this enables us to model the accuracy of the force wrench implementation as an angle-dependent value and velocity-independent. Keep in mind that this only holds when all rotors are spinning at the same velocity. The accuracy of the force implementation of the wrench is then 1 minus this value. The accuracy for each of the angles is taken, and a curve is fitted to the results. This can be seen in Figure 5.12. In the figure can be seen that the accuracy at low tilt angles is less accurate then the accuracy at higher tilt angles. According to the curve, the optimal accuracy is achieved at 41 degrees. As the force in the x- and y-directions are cancelled when all the rotors are spinning, a different method will be used to evaluate these. Using this curve as a simple way to model the force accuracy in the z-direction of the wrench does not over complicate the model while achieving beneficial results. However, this method only gives an insight into the accuracy of the force of the total wrench. To create a good model, it is beneficial to get an insight into the effect of a single rotor on the accuracy of the wrench.

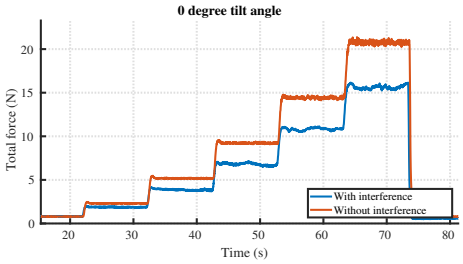

(a) For $\alpha = 0$ degree.

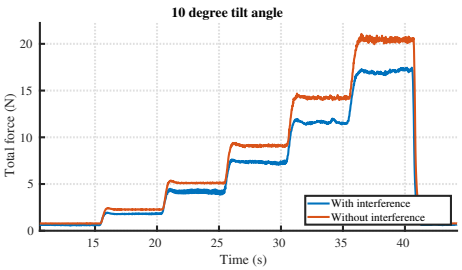

(b) For $\alpha = 10$ degree.

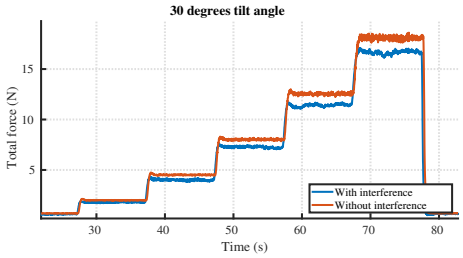

(c) For $\alpha = 30$ degree.

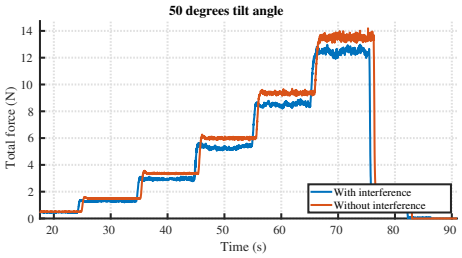

(d) For $\alpha = 50$ degree.

Figure 5.10: The total force on the platform with interference and the force achievable via the allocation matrix for different angles.

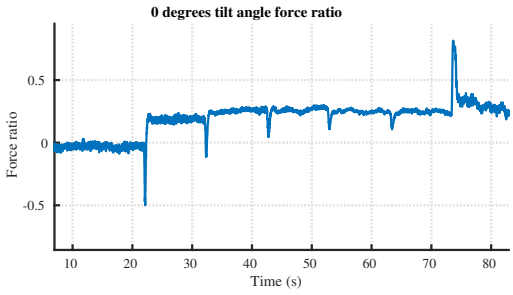

(a) For $\alpha = 0$ degree.

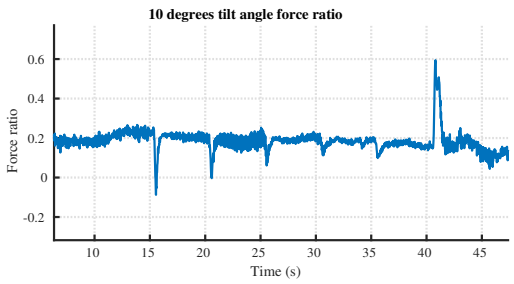

(b) For $\alpha = 10$ degree.

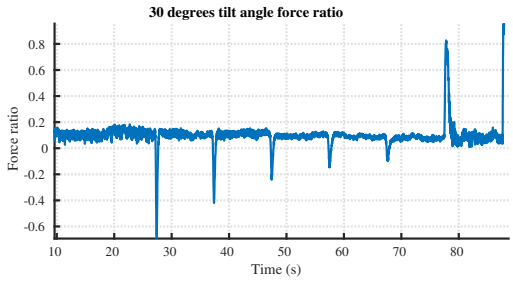

(c) For $\alpha = 30$ degree.

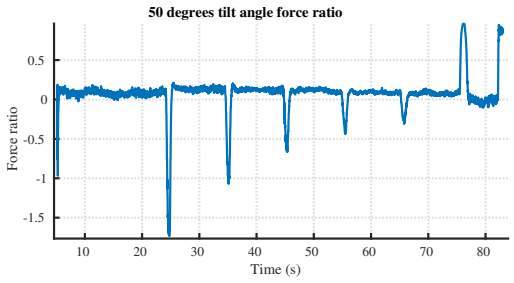

(d) For $\alpha = 50$ degree.

Figure 5.11: Ratio between the force loss by interference over the measured force with interference at different angles.

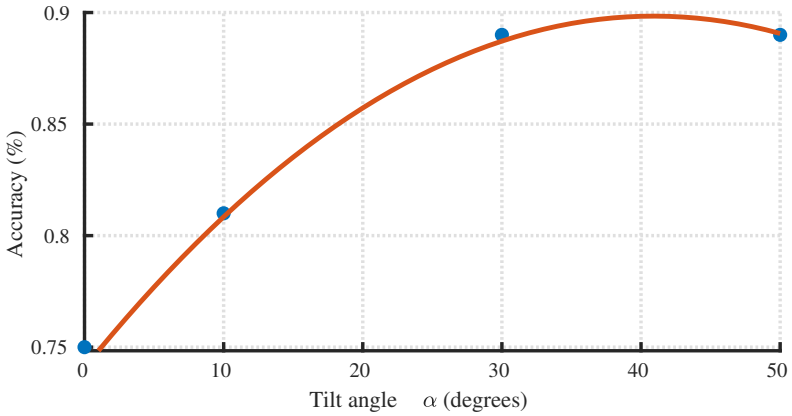

Figure 5.12: Wrench accuracy curve of the force at the CoM predicted with a simple model against measured values.

5.5.2 Force components of the wrench execution of a single rotor

From Equation 2.5, it can be seen that the force exerted by a rotor is directly translated to the body. By investigating the difference between the force generated with and without interference, we can determine the wrench accuracy of the force for a single rotor. As we have seen that the top rotors are not affected by interference, we will only consider the bottom rotors. By using the Equation 2.8, the measurements of a single rotor at 0 degree α can be transformed to 10, 30 and 50 degrees tilt angle as a benchmark against the measurements with interference. We use the second setup with the single rotor on the force-torque sensor and spin the rotor at 120 Hz while increasing all other rotors in a stepwise fashion from 20 Hz to 120 Hz with 20 Hz increments. Figure 5.13 shows the x, y, and z components of the force at different tilt angles compared to the benchmark.

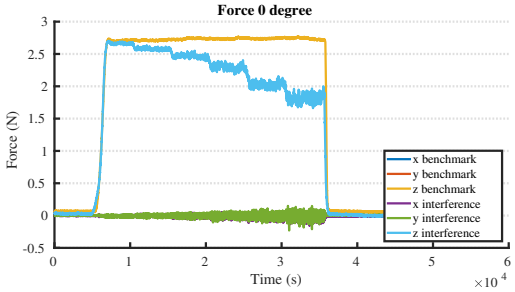

(a) For $\alpha = 0$ degree.

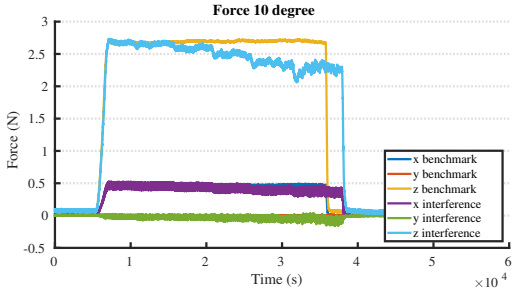

(b) For $\alpha = 10$ degree.

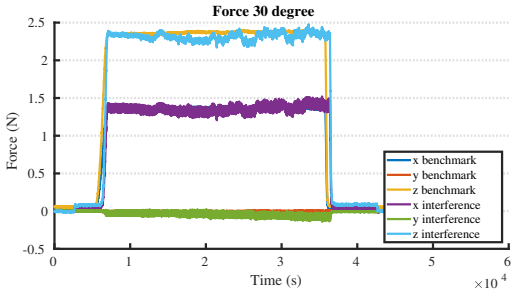

(c) For $\alpha = 30$ degree.

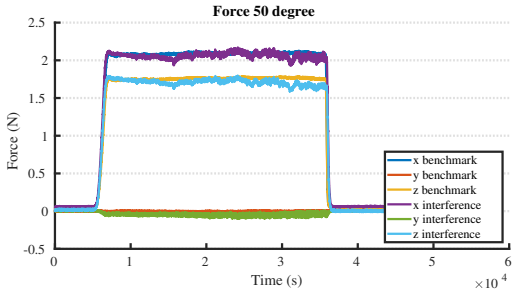

(d) For $\alpha = 50$ degree.

Figure 5.13: Force with interference compared to the benchmark force without interference for the x-, y- and z-direction.

From the comparison in Figure 5.13, we take the average of the forces for each of the different rotor velocities at different angles. The difference between the force with and without interference can be seen in Figure 5.14. This follows what we have seen in Figure 5.12 for the CoM. As the angle increases, the difference between the force in z-direction decreases. The difference in force for small tilt angles α in the x and y directions is very small compared to the net difference for the z direction. From this can be said that, for the wrench execution, the most significant difference is created in the z direction.

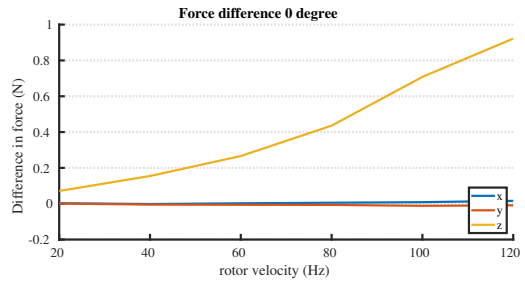

(a) For $\alpha = 0$ degree.

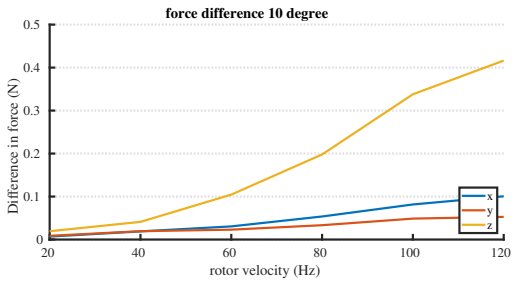

(b) For $\alpha = 10$ degree.

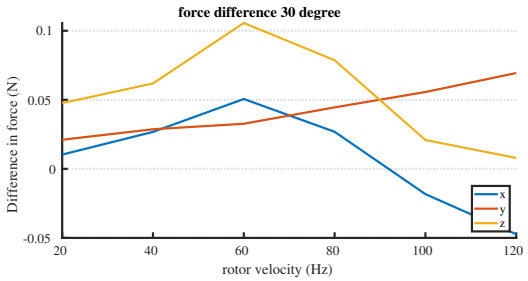

(c) For $\alpha = 30$ degree.

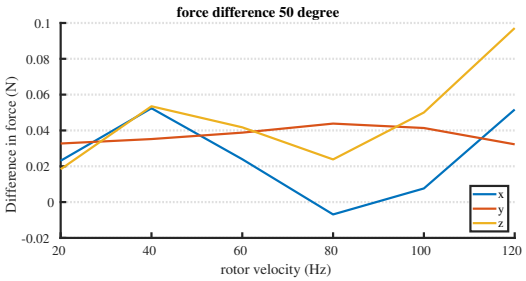

(d) For $\alpha = 50$ degree.

Figure 5.14: Difference between the force with interference compared to the benchmark force without interference for the x-, y- and z-direction for each step of increasing interference.

From these figures, we can calculate the accuracy in terms of the percentage difference between the wrench with and without interference. The measured rotor is the rotor that tilts around the y-axis. We can see in Figure 5.13 that the force in the y-axis of the rotor without interference is near 0. In the experiments with interference, a small amount of force is measured in the y-direction (maximum 0.07 N for the 30 degree tilt angle). This results in a significantly higher percentage difference in accuracy but is only a very small net amount of error. We therefore only show the difference in the x and z direction. This difference can be seen in Figure 5.15. In Figure 5.15a, the accuracy of the force in x is very different from the accuracy of the force in z. This is expected as the force in x of the benchmark should be close to 0 N with small changes in the force resulting in big percentage differences. For the other figures where the net force in x is bigger, the percentage difference is more representative. We can see that both forces result in similar differences from the forces without interference. For 0 and 10 degrees there is a significant difference in the force, however, the force in 30 and 50 degrees has only a few percent difference. The force in the y-direction was not plotted for clarity of the overall figure. The force in the y-direction has around a -80 % difference for α 10, 30 and 50 degrees while the difference goes up to 1500 % in the case of $\alpha = 0$.

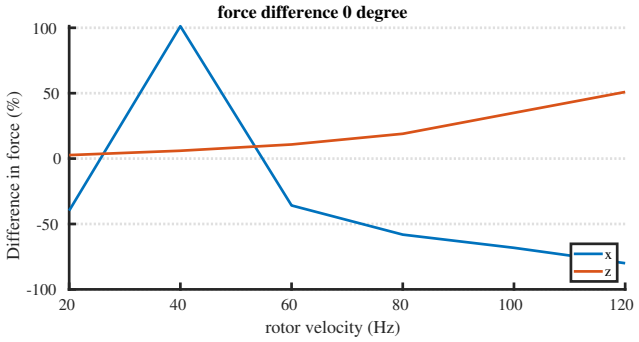

(a) For $\alpha = 0$ degree.

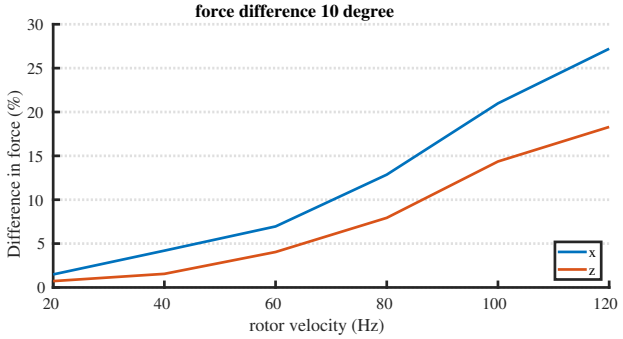

(b) For $\alpha = 10$ degree.

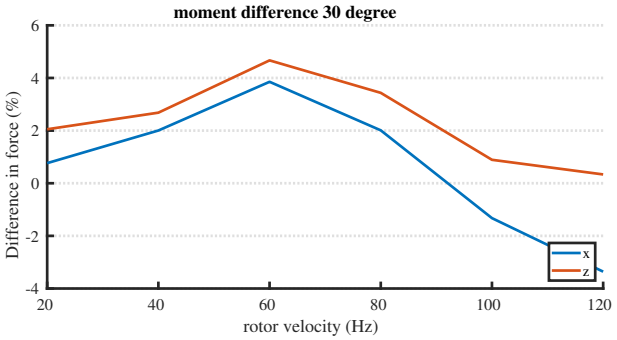

(c) For $\alpha = 30$ degree.

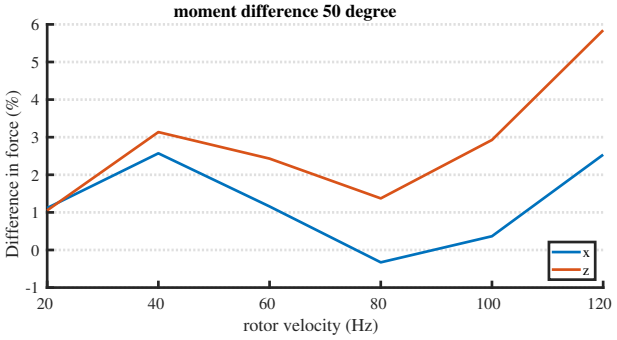

(d) For $\alpha = 50$ degree.

Figure 5.15: Difference between the force with interference compared to the benchmark force without interference in percentage for the x-, y- and z-direction for each step of increasing interference.

5.5.3 Moment components of the wrench execution

To find the accuracy of the torque execution on the body, the same experiment as the force on the CoM cannot be performed. This is because, when all the propellers of the platform are spinning, the moments around the CoM are 0. If this were not the case, the platform would rotate at hovering. To investigate the accuracy of the moment, we transform the moments on a single rotor to the body, similarly to the second part of the wrench execution of the force. First, we need to understand what is happening to the moment on a single rotor when the rotor is subjected to aerodynamic interference.
To get an understanding of this, the moment in all directions is investigated of a rotor spinning at 120 Hz in the case where there is no interference compared to a rotor spinning at the same rotor velocity, which is subjected to interference. The interference is created by all other rotors stepping from 20 Hz to 120 Hz in 20 Hz stepwise increments. Figure 5.16 shows the moments for the smallest and biggest tilt angles of 0 degrees and 50 degrees α without interference. The moment without interference at an α of 50 degrees can be seen in Figure 5.16b. This figure shows that there is a moment in all 3 DoFs. This is unexpected, as in the configuration of the OmniMorph, the rotor is pointing in the x-z-plane with an angle of 50 degrees away from the z-axis. This means we would not expect any moment around the y-axis. The suspected reason for this is that in the setup (as can be seen in Figure 5.1b) the force torque sensor is attached to the rotor with a 3D-printed bracket which determines the 50 degree angle. The line created along z_{P_i} of the rotor does not go through the origin $\mathcal{O}_S$ of the sensor. This can be seen in Figure 5.17. Similarly as the Equation 2.6 for the moment from the propeller to the body, the forces at a small distance from the force torque sensor are hypothesized to result in a small moment around the y-axis. This explains why we see that there is a moment around the y-axis which is not present in the 0 degree case as the propeller is pointing directly towards the force torque sensor.
This can be confirmed by comparing the norm of the sensor in both cases without interference and the 50 degree case where the y-axis is left out. This can be seen in Figure 5.18. It can clearly be seen that the norm matches when the y-axis is not taken into account. We choose to neglect the moment around the y-axis of the force torque sensor when calculating the accuracy of the wrench on the body.

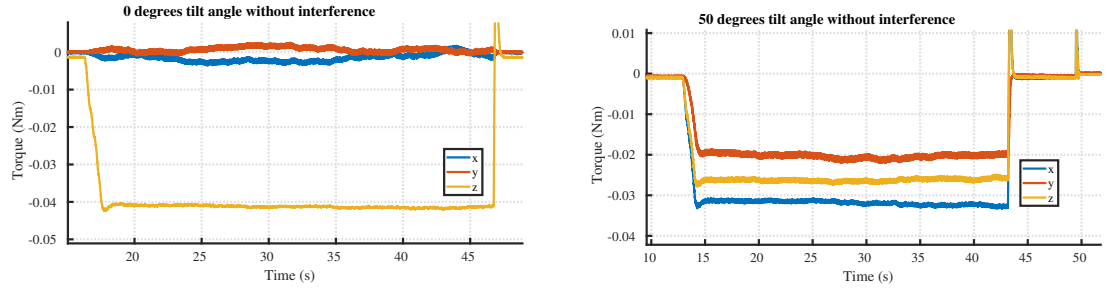

(a) For $\alpha = 0$ degree without interference.

(b) For $\alpha = 50$ degree without interference.

Figure 5.16: Moments for 0 and 50 degrees without interference.

In the case of the α of 0 degrees, all the moment is expected to be directed towards the z-direction. This is confirmed in Figure 5.16a, where there is no interference. However, once the rotor is subjected to interference in Figure 5.19a, there is a small moment around the x and y-direction. Most of the noise in the measurement of these moments can be attributed to vibrations in the sensor, but it can be seen that even with the vibrations, these moments deviate from 0. As the interference increases, the moment tilts slightly towards the outside of the Omnimorph. A possible explanation for this is that the part of the propeller closer to the

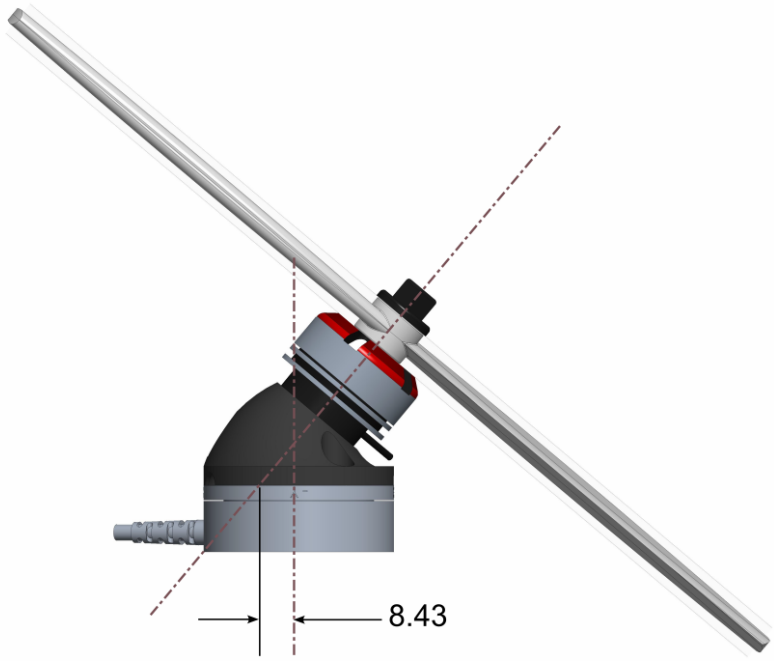

Figure 5.17: Schematic of the rotor on the force torque sensor. The line through the rotor does not go through the middle, which means that the force of the rotor will create a torque in the sensor measurements.

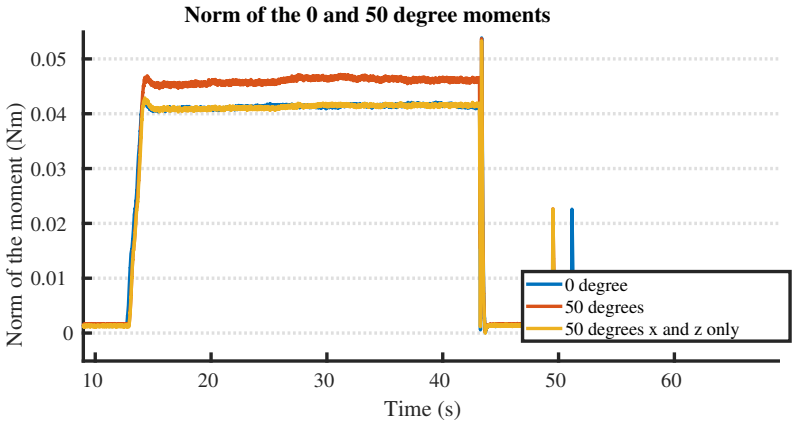

Figure 5.18: Difference between the norm of the moment at 0 degrees against the norm at 50 degrees vs the norm taking only x and z into account.

other rotors (on the inside of the OmniMorph) is more affected by the interference created than the part on the outside. That results in a local reduction in c_τ, which tilts the moment outward.

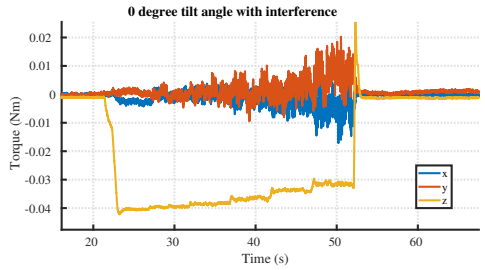

(a) For $\alpha = 0$ degree with interference.

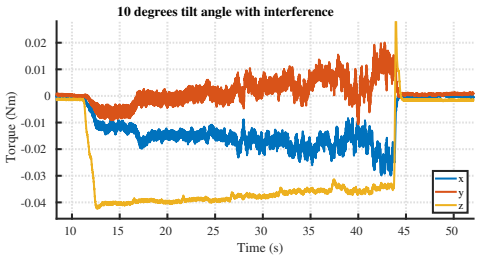

(b) For $\alpha = 10$ degree with interference.

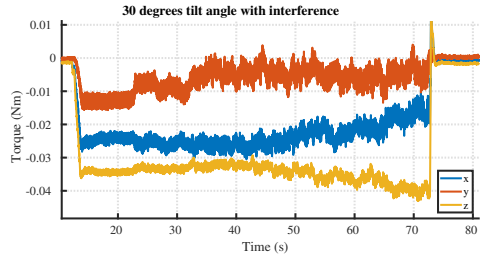

(c) For $\alpha = 30$ degree with interference.

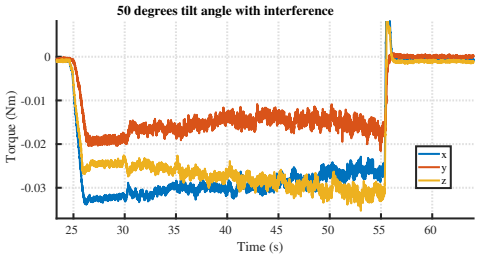

(d) For $\alpha = 50$ degree with interference

Figure 5.19: Moment in 3 DoF for α of 0, 10, 30 and 50 degrees with interference.

The accuracy of the moment can be calculated by comparing the moment without interference to the moment with aerodynamic interference. This must be calculated from the body frame as the total body moment has force and moment components (as seen in Equation 2.6). From Figure 5.19d, it can be seen that the moment changes direction over time. The moment on the body can be calculated by transforming the wrench from the sensor frame to the body frame using Equation 2.8. Figure 5.20 shows the transformed moments to the body for different tilt angles for the benchmark moment without interference and the moment with interference. The accuracy was investigated for each of these moments at the different rotor velocities. This is shown in Figure 5.21 where the deviation from the moment due to aerodynamic interference is plotted. As can be seen in the figure, for the lower tilt angles, the accuracy of the moment around y follows the moments around x and z, however, at higher tilt angles, when the error in the moment around y for the rotor was more prevalent, the total error of y in the wrench accuracy is also further away from the accuracy of the x and z moments.

5.6 Possible solutions to minimize the effect of aerodynamic interference

In order to prevent or minimize the effects of the propellers on each other, three different solutions are proposed. These solutions are discussed and for every solution, it is investigated if it could possibly lead to a more efficient platform. The first two solutions are related to changing the platform in some way. The last solution is to see if there exists an α which is more energy efficient than the simulated α of 0 degrees.

5.6.1 Increasing the distance between the propellers

The first design choice is to increase the distance between each of the propellers. This would add more space in between the propellers which would let the air pushed by the top propeller

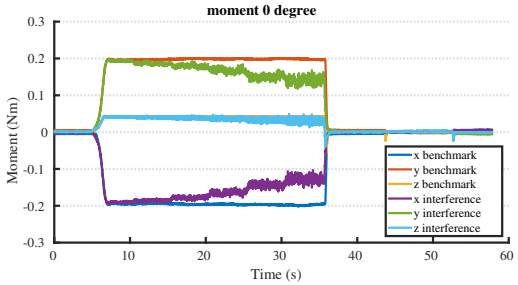

(a) Moment of $\alpha = 0$ degree with interference compared to the moment without interference.

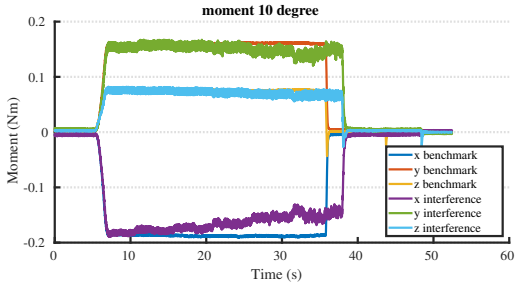

(b) Moment of $\alpha = 10$ degree with interference compared to the moment without interference.

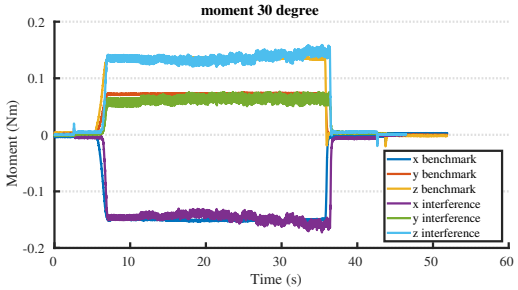

(c) Moment of $\alpha = 30$ degree with interference compared to the moment without interference.

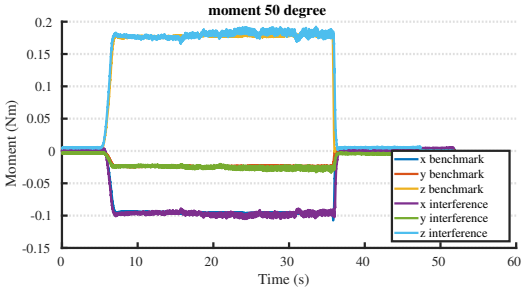

(d) Moment of $\alpha = 50$ degree with interference compared to the moment without interference.

Figure 5.20: Comparison of the moment on the body in 3 DoF for α of 0, 10, 30 and 50 degrees with and without interference.

slow down and stabilize before sending it through the bottom propeller. Figure 5.22 shows a representation of the setup of the experiment performed. For this experiment, the second setup was used and the rotor attached to the force torque sensor was lowered by both 20 cm and 40 cm to compare the effects of aerodynamic interference at these distances.
The measured lowered propeller was then spun at 120 Hz while the top propeller was spinning from 20 Hz to 120 Hz and increased by 20 Hz in a stepwise fashion. The results from this experiment can be seen in Figure 5.23. Note that the distance of 0 cm in the figure corresponds to the original design of the OmniMorph, which has its propellers spaced at a distance of 25 cm between each other. What we can see from the figure is that increasing the distance between the propellers decreases the amount of aerodynamic interference the bottom rotor experiences. At an extra distance of 40 cm, the force exerted is increased from 1.89 N to 2.30 N. The propeller without interference exerts 2.85 N of force. This means that an increase of propeller distance of 40 cm results in a 43% reduction of aerodynamic interference. An increase of only 20 cm results in a 28% improvement in interference. What is important to note is that increasing the distance between the propellers also makes the drone heavier due to the additional material needed. This means that it will require more power to fly. Additionally, the rotors account for 360 g out of the total 1.25 kg of the drone. Increasing the distance from the CoM will also change the mass moment of inertia. From Equation 2.6, it is also possible to see that the moment generated by the propellers will also change. The force exerted at low speed for the propeller lowered by 40 cm is also lower than in the other cases. It is unknown why this is the case. It could be that the sensor was tared incorrectly, the longer power cables created a power loss, or another reason.

5.6.2 Position change of bottom propellers

The second way to try to minimize the influence of aerodynamic interference is to modify the platform in such a way that the bottom propellers are minimally affected by the top propellers.

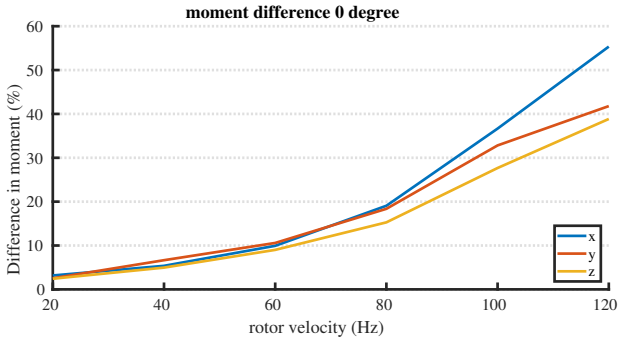

(a) Percentage difference of the moment of $\alpha = 0$ degree with interference compared to the moment without interference.

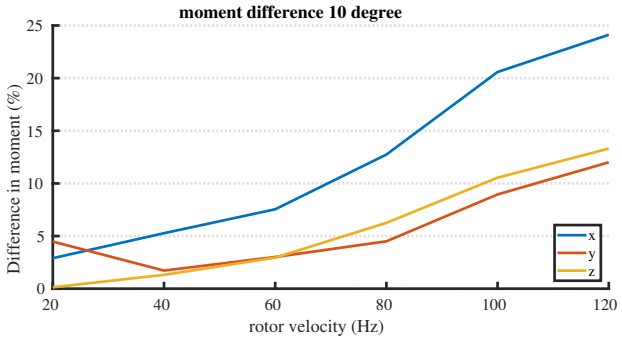

(b) Percentage difference of the moment of $\alpha = 10$ degree with interference compared to the moment without interference.

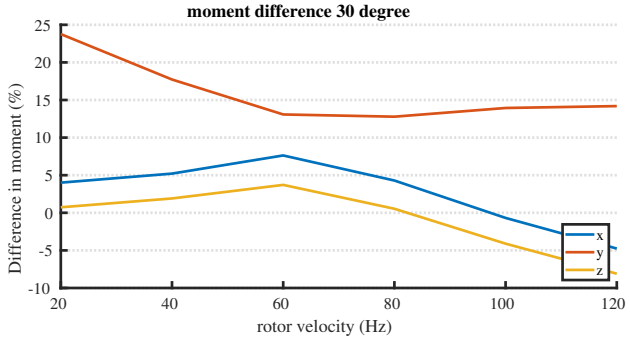

(c) Percentage difference of the moment of $\alpha = 30$ degree with interference compared to the moment without interference.

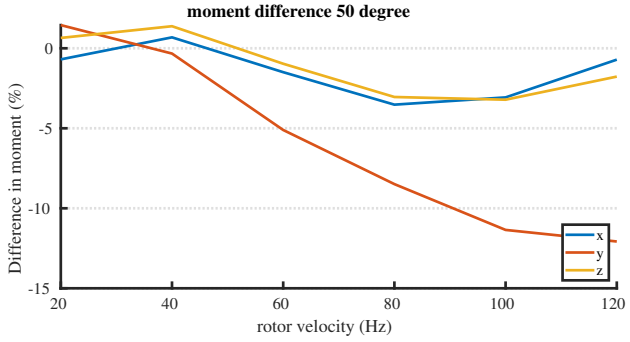

(d) Percentage difference of the moment of $\alpha = 50$ degree with interference compared to the moment without interference.

Figure 5.21: Percentage difference of the moment on the body in 3 DoF for α of 0, 10, 30 and 50 degrees with and without interference.

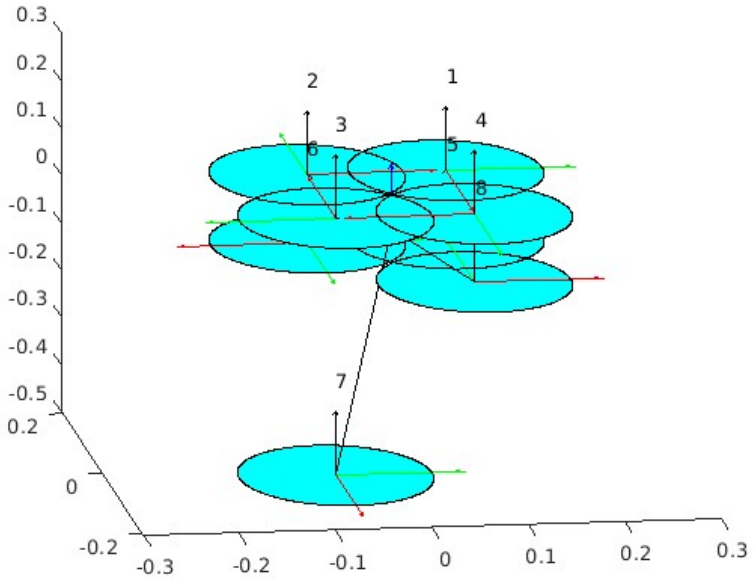

Figure 5.22: Representation of increasing the distance between the rotors. Due to the setup limitations, only one rotor was brought downwards.

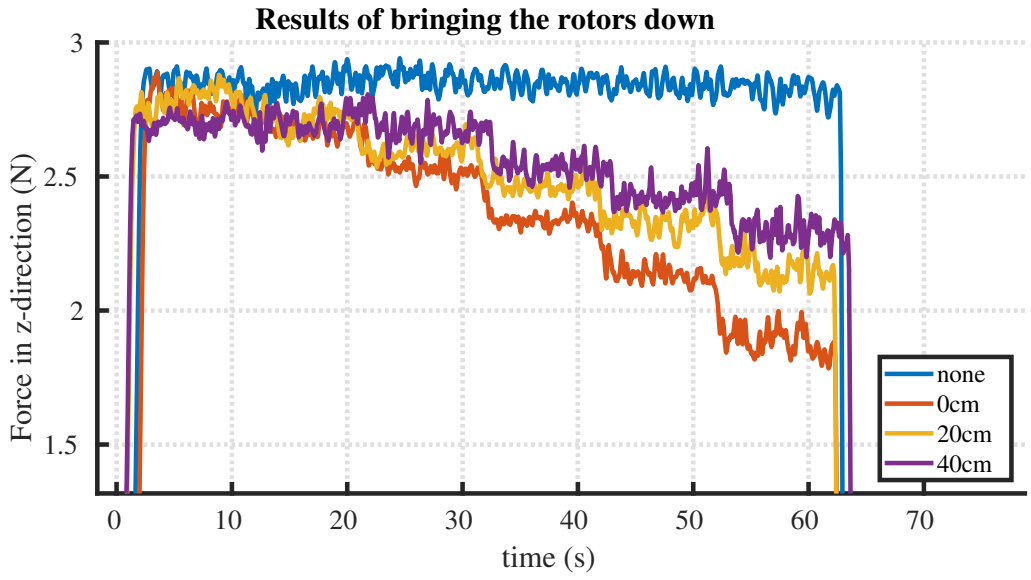

Figure 5.23: Figure showing the effect of increasing the distance between the propellers. The different distances of 0 (orange), 20 (yellow) and 40 cm(purple) have been compared to the situation without any aerodynamic interference (blue).

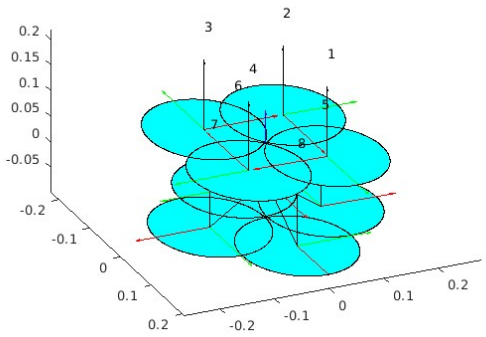

(a) Side view of the newly proposed rotor configuration of the OmniMorph.

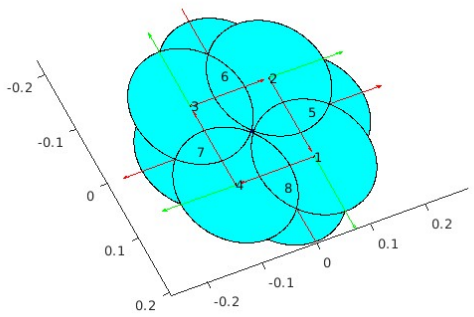

(b) Top view of the newly proposed rotor configuration of the OmniMorph.

Figure 5.24: Side view and top view of the newly proposed rotor configuration.

The proposed solution for this is to change the position of the rotors in such a way that the bottom propellers are not in line with the top propellers anymore. This is done by keeping the same distance from the CoM but changing the position of the rotors in such a way as to minimize the area of the bottom propeller that overlaps with the cylinder projected along the z-axis in the propeller frame by the top propellers. A representation of the OmniMorph with the change of the bottom propellers can be seen in Figure 5.24b and 5.24a.

Changing the platform in this way would also change the allocation matrix of the platform. The choice was made to keep the tilt of the propellers around the same axis as the original OmniMorph. The rank of the allocation matrix in this configuration is 6, therefore the platform is at least FA. For the platform to also be OD, it should be able to hold its weight in every orientation. We first explore if this configuration of the drone results in less aerodynamic interference than the original configuration. To see this, the second setup with the force torque sensor on the bottom rotor is used with an angle α of 0 degree. The bottom rotor has been placed at the location of the rotor in the newly proposed configuration. The measured propeller is spun at 120 Hz while the other rotors are spun with a velocity of 20 Hz to 120 Hz with a stepwise increment of 20 Hz. This is compared with the same experiment done with the original configuration and experiment with the single propeller spinning at 120 Hz without any interference. This comparison can be seen in Figure 5.25. From the figure, we see that the change of position shows no improvement at higher speeds. At lower speeds, the interference on the rotor at a changed position is worse. The hypothesis on this is that, because the rotor at the new position is close to two propellers, the measured rotor was affected by the interference created by both propellers. If the trend of the lines between the new position and the original position continues, there could be an amount of interference for which the new position is more beneficial than the current position.

5.6.3 Finding the optimal alpha

The third and final solution proposed in this thesis is to investigate whether there is an α for which the power needed for hovering is less than the theoretical optimal α of 0. The reason that there could be a more efficient solution than α at 0 degree is that, with an increase in α, the airflow generated by the top propeller is directed further and further away from the bottom propeller. This could mean that the effect of the aerodynamic interference is reduced with increased α and subsequently, there could be an α for which the power needed to hover is less than the 0 degree α case. The power for a drone at a steady rotor velocity has been described

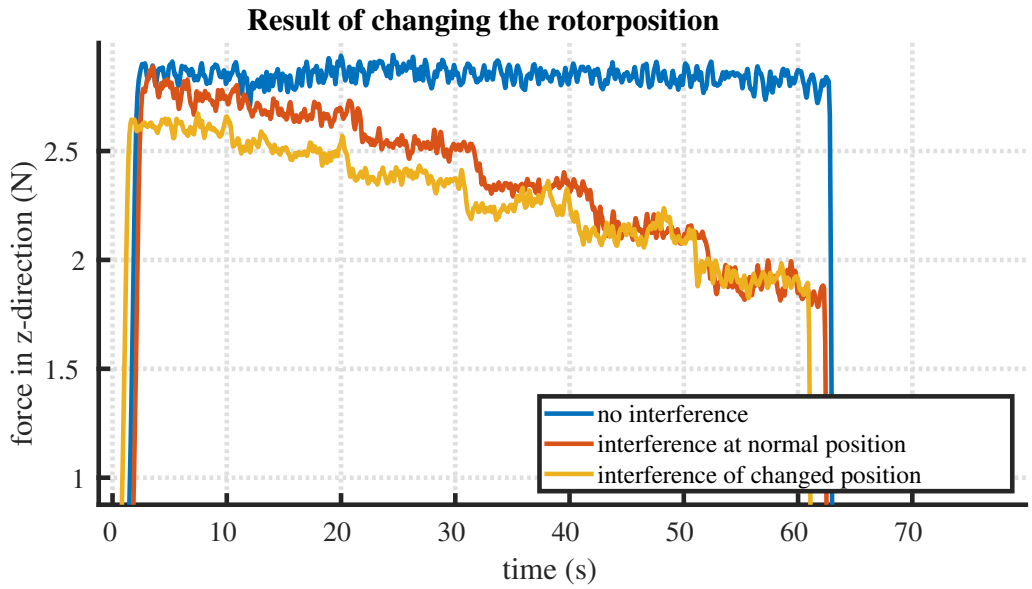

Figure 5.25: Figure showing the effect of changing the position of the rotor. The change in position (yellow) has been compared with the position in the normal configuration with interference (orange) and without interference (yellow).

by Equation 2.15.
We first define the hovering velocity for the different α. From Figure 5.10 it can be seen that the hovering velocity of the 50 degrees α tilt angle is around 120 Hz. We can safely say that this will not be a more optimal tilt angle. Using the first setup and increasing the rotor velocity from 95 Hz to 120 Hz in 5 Hz steps, the rotor velocity can be measured for which the platform will hover. Figure 5.26 shows the hovering velocity for the 0, 10 and 30-degree tilt angles. These have been found to be 105, 104 and 105 Hz respectively. Interesting to note is that the hovering velocity of the platform first decreases with α and then increases again.
The next step is to compute the power needed to hover for each of the hover velocities. As the platform is subjected to aerodynamic interference, the top rotors will output a different moment to the bottom rotors. The mechanical power exerted by the top rotors can be calculated with the moment output by a rotor without interference. Using the second setup, we spin a rotor from 40 Hz to 200 Hz with 20 Hz intervals and fit a line to the moment output of the propeller. Figure 5.27 shows this fit.
Using Equation 2.15, we can calculate the power output at hovering for the four top propellers. For the bottom four propellers, we can fit a similar line to the moment for different tilt angles when interference occurs. We first evaluate the change in moment with different amounts of interference. This can be seen in Figure 5.28. Using this figure and Figure 5.27, we can calculate the moment when interference occurs. The final estimation for the moment at different rotor velocities for different tilt angles can be seen in Figure 5.29.
The total mechanical power exerted is the sum of all eight rotors together. This comes out to 140.88 W for the 0 degree α, 152.01 W for the 10 degree α and 159.56 W for the 30 degree α. This means that even with aerodynamic interference, the most optimal α in terms of power efficiency is still at $\alpha = 0$. This is not equal to the total amount of power output for hovering but only the mechanical power of the rotors. The full platform will lose power in the form of heat, and other components are not taken into account.

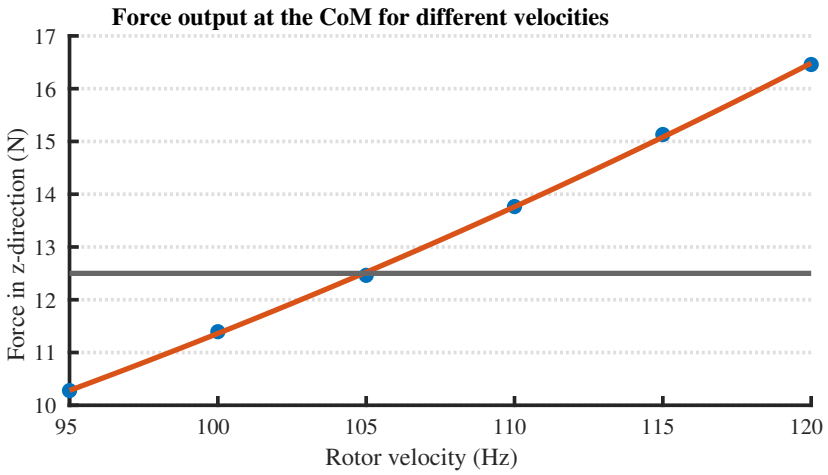

(a) Force output at different rotor velocities for the 0-degree tilt angle.

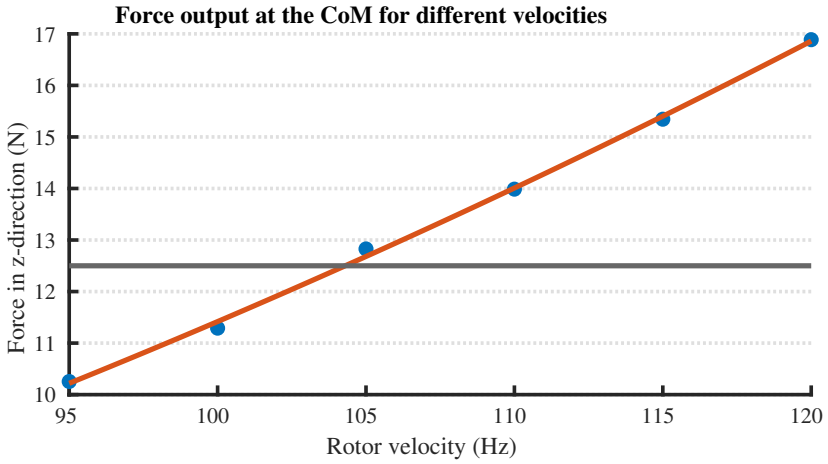

(b) Force output at different rotor velocities for the 10-degree tilt angle.

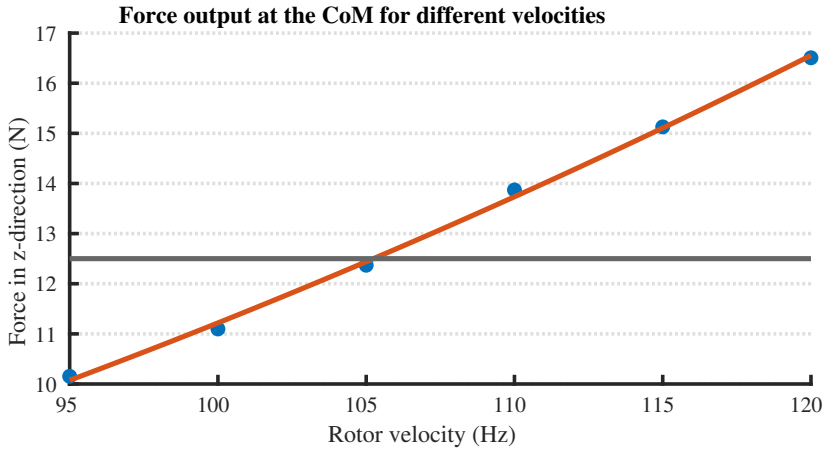

(c) Force output at different rotor velocities for the 30-degree tilt angle.

Figure 5.26: Hovering rotor velocity estimation for the 0, 10 and 30 degrees tilt angles.

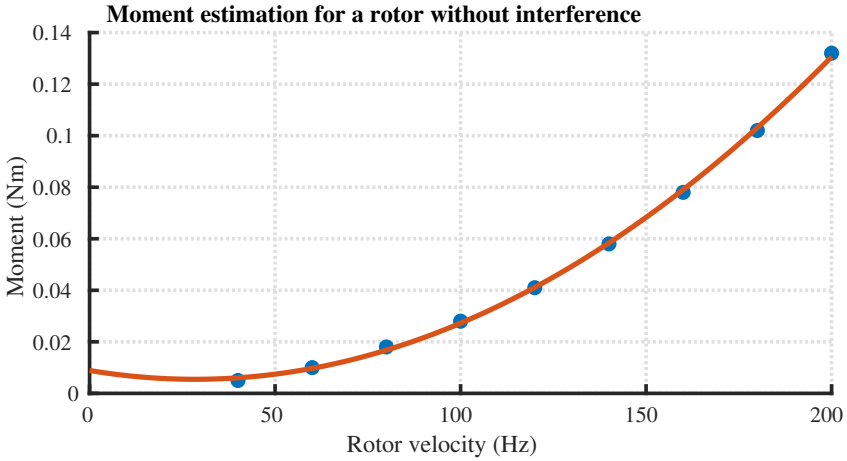

Figure 5.27: Estimation of the norm of the moment for a rotor without interference by fitting the measured data.

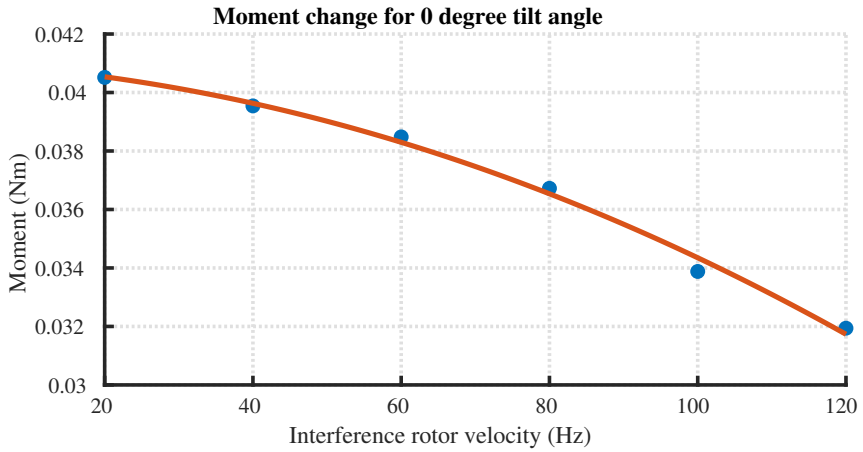

(a) Estimation of the change in the moment for a rotor spinning at 120 Hz at $\alpha = 0$ with interference by fitting the measured data.

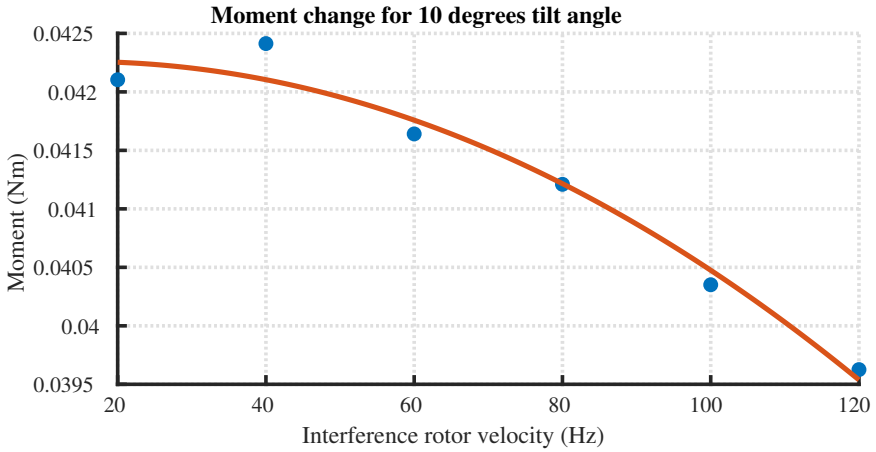

(b) Estimation of the change in the moment for a rotor spinning at 120 Hz at $\alpha = 10$ with interference by fitting the measured data.

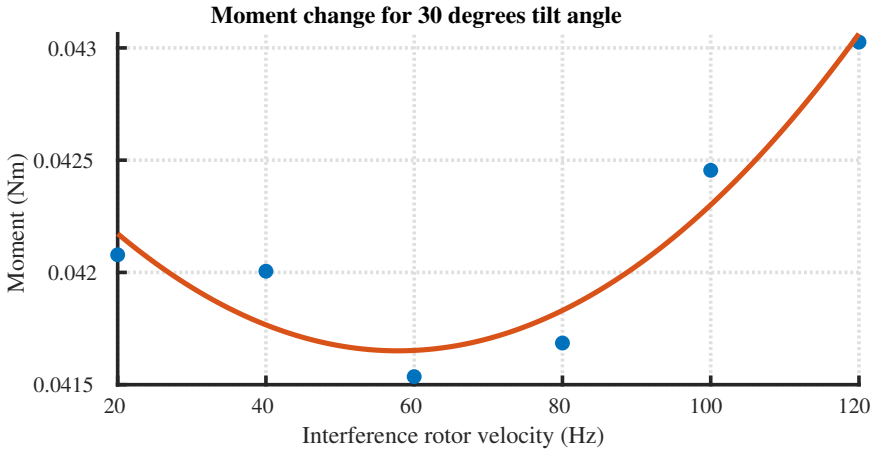

(c) Estimation of the change in the moment for a rotor spinning at 120 Hz at $\alpha = 30$ with interference by fitting the measured data.

Figure 5.28: Estimation of the change in the moment for a rotor at different angles for different amounts of interference. The total moment was measured by taking the norm.

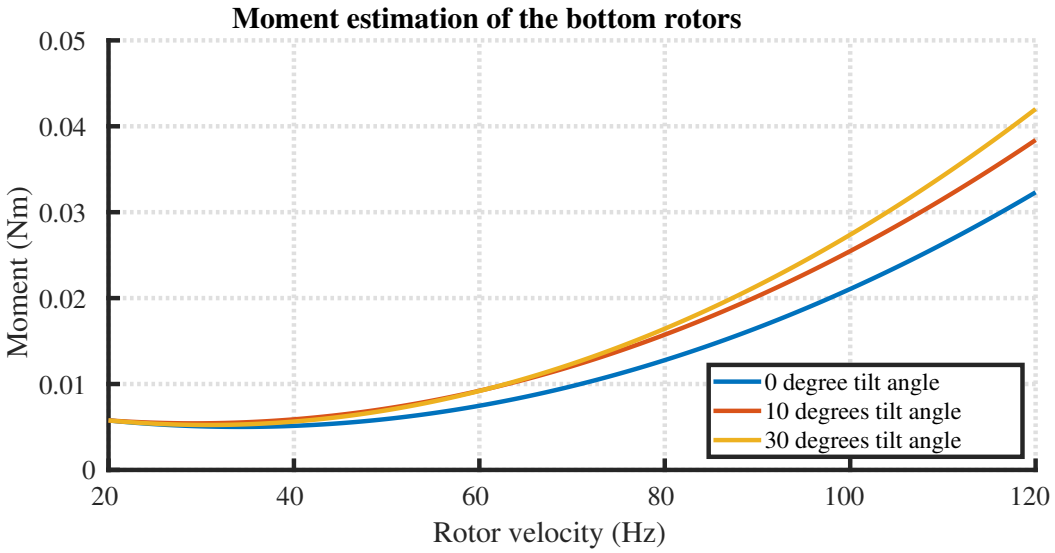

Figure 5.29: Estimation of the norm of the moment for a rotor with interference at different tilt angles.

6 Conclusions and Recommendations

To conclude this thesis, the research questions will be answered. Based on this, recommendations will be given.

6.1 Conclusions

How accurate is the wrench execution when alpha is changed with the wrench mechanism? Is some alpha better and more accurate?

From Figure 5.12, a curve was created for the accuracy of the force execution of the CoM, which shows that the optimum α in terms of accuracy is at a tilt angle of 41 degrees. Figure 5.15 shows what is happening in a single rotor which gives a more concrete view of the force accuracy. As the tilt angle α around y increases, the accuracy of the force also increases. Especially for lower angles, an increase in interference results in a decrease in force accuracy of the wrench execution.
In Figure 5.21, it can be seen that the moment execution of the wrench due to a single rotor on the body follows the same trend. As the tilt angle α around y increases, the accuracy of the wrench execution increases. With an increasing amount of aerodynamic interference, the accuracy of the moment part of the wrench decreases.
For the total wrench, it can therefore be said that, with increasing α and decreasing amounts of interference, the wrench execution becomes more accurate.
The force execution in the y direction can best be shown by Figure 5.14 where the deviation from the force without interference is less than 0.07 N in most cases, which is very small. Assumptions were made for the moment execution around the y-axis due to the way the measurements were performed. As the tilt angle increased, the moment around y of the measurement of the force-torque sensor increased. It is hypothesized that the assumptions on the force torque sensor measurements are what causes the difference in the moment around the y-axis in Figure 5.28c and 5.21d.

Is there a design modification that would lead to an optimal value of alpha corresponding to a lower value of the control input at hovering compared to the optimal alpha of the current prototype?

Two design modifications were proposed where the position of the rotors is changed, and one design optimization was proposed where the optimal α could be different than $\alpha = 0$. The first design modification, increasing the distance between the rotors, decreases the amount of aerodynamic interference. At an additional rotor distance of 40 cm, the aerodynamic interference of the bottom rotor is reduced by 43 %. This is a significant amount. However, an increase in distance between the rotors will result in additional mass due to a larger frame. A larger frame could potentially need extra reinforcement which results in even more mass. Bringing the rotor down by 20 cm could be a better option as this results in a 28 % improvement on the maximum measured interference. This is less improvement but will, at the same time, require less additional mass. More research needs to be done to investigate what the optimal rotor distance is in relation to the additional mass gained.
Changing the position of the bottom propellers does not change the aerodynamic interference positively. In Figure 5.25, it can be seen that the force exerted by the rotor is similar at higher amounts of interference, while at lower amounts of aerodynamic interference, the position change results in a worse amount of force exerted.
The optimal α in terms of energy efficiency does not change with regards to the model without

interference and is at $\alpha = 0$ with a rotor velocity of 105 Hz. This results in a minimum mechanical power necessary for hovering of 140.88 W. At a tilt angle of 10 degrees, the hovering rotor velocity is lower but results in a higher amount of total mechanical power needed to hover.

6.2 Recommendations

During this thesis, the effects of aerodynamic interference on the rotors of the OmniMorph were analyzed. It has been seen from the results that the effects of aerodynamic interference are present during the operation of the OmniMorph. More research needs to be done to derive a specific model for these effects. It is recommended for this model to change the c_f and c_τ based on the velocity of the rotor itself and the velocity of the rotor that is spinning above it (if there is one). The α of the OmniMorph is also important to consider. These are the parameters that seem most important to derive a more accurate model for the OmniMorph at steady-state hovering conditions. At steady-state hovering conditions, the aerodynamic interference could also be directly approached by multiplying the wrench with the curve described in Figure 5.12. The downside is that this would only solve the issue for the states in which the orientation of the platform is upright, and all propellers are spinning at similar speeds. The upside is that it is a very simple second-order curve dependent on only the tilt angle α.

For a more general approach, which would include the OmniMorph changing orientation, more parameters and variables should be taken into account. The distance of the rotors from each other and the diameter of the rotors themselves, and the angle at which they are oriented towards each other are some suggestions for parameters to take into account. The ratio between interference from other rotors versus interference from the rotor directly above could be added. This effect can be seen in Figure 5.7 where, at lower velocities, the aerodynamic interference of other rotors has a more significant influence than it has at higher rotor velocities.

Due to time limitations, the accuracy of the wrench implementation for 20 degrees and 40 degrees α was not done. In the future, doing the experiments to complete Figure 5.12 is advised. The reason behind this is that, according to the curve, the optimal α for the wrench implementation is at 41 degrees. My intuition says this is not the case because in Figure 5.7, there is aerodynamic interference due to all other rotors except the one above the measured rotor. My theory is that, above around 60 Hz aerodynamic interference, the top rotor is the dominant rotor in providing aerodynamic interference, and as α becomes larger, this effect diminishes until the other rotors are the dominant effect. This would split the curve of Figure 5.7 in such a way that between α at 0 and some angle under 30 degrees, it will follow a certain curve until it reaches the angle where the other rotors are dominant and the curve flattens.

Most experiments were done with a rotor velocity of 120 Hz. This was done to compare the different experiments with each other. The velocity was taken because the OmniMorph would sometimes shut down because it was pulling more than 45 A from the power supply when all rotors were spinning at higher speeds. This could be a power supply issue and could be resolved by using the battery. As a rotor velocity of 120 Hz was shown to be the hover velocity of the OmniMorph at 50 degrees α, there was no need to go much higher for the experiments performed during this thesis. Something which could be interesting to investigate is what happens when the measured rotor spins at different velocities. We can then see how the rotor velocities relate to each other. Is the bottom rotor always affected in the same way by the top rotor, or is it the difference in rotor velocities that determines the amount of interference? The answer to this question could extend the model of aerodynamic interference even further.

Two different solutions to minimize the aerodynamic interference were proposed. These were tested separately from each other. Increasing the distance between the rotors and changing the position could be implemented in the same design. The distance between the rotors would decrease the area projected by the top propeller on the bottom propellers, which could potentially reduce the aerodynamic interference. The platform would become heavier due to the increased size of the OmniMorph. Additionally, implementing the tilting mechanism becomes more complicated when the position of the bottom rotors is changed.

In the future, a machine learning algorithm could be trained to incorporate aerodynamic effects in the model. More research needs to be done to achieve this. The model could at first be used to model all the effects present at a steady state hovering for different tilt angles. It could then be extended for flight in all different orientations. I think this would be very interesting for future research.

During the accuracy of the moment part of the wrench, as the tilt angle increased, an additional moment was created due to the force. For future experiments, it would be beneficial to change the design of the 3D-printed part that attaches the rotor to the force torque sensor. My recommendation would be to always keep the rotor itself on the 3D-printed part, which sits at 0 degree α attached to the force-torque sensor and create an additional part that tilts the rotor and the force-torque sensor together. This way, the sensor will not measure any additional torques due to the force.

Last of all, my suggestion is given with regard to a model for aerodynamic interference. For a simple yet possibly more accurate model of OmniMorph, which takes into account the aerodynamic interference without orientation change, the proposed model change is to change c_f and c_τ in the following ways for the rotors influenced by aerodynamic interference (rotor 5, 6, 7 and 8 from Figure 2.1):

$$c_f(\alpha, u_{\lambda-4}) = c_{f_0} - \Delta_f(\alpha) u_{\lambda-4} \tag{6.1}$$

$$c_\tau(\alpha, u_{\lambda-4}) = c_{\tau_0} - \Delta_\tau(\alpha) u_{\lambda-4} \tag{6.2}$$

In Equation 6.1, we consider the c_f to be dependent on the tilt angle α and the rotor velocity of the rotor situated directly above the rotor considered $u_{\lambda-4}$. From Figure 5.7, it can be seen that this is the rotor with the most influence on the aerodynamic interference. c_{f_0} is the base coefficient of force from Figure 5.4a. Depending on the tilt angle and the velocity of the rotor directly above the rotor considered, the base coefficient will be diminished. $\Delta_f(\alpha)$ is an angle-dependent second-order equation that looks similar to the fitted second-order line in Figure 5.12. At low α, $\Delta_f(\alpha)$ will be high and as α increases, $\Delta_f(\alpha)$ will diminish. The curve can be fitted on the data of Figure 5.15. From Figure 5.14 it can be seen that the net difference in force for the x and y components are small. The model could be simplified even further by only considering the change in c_f of the force in the z-direction on the body.
Equation 6.2 is based on the same principle. The c_{τ_0} is the base coefficient of drag from Figure 5.4b. The $\Delta_\tau(\alpha)$ is another second-order function that can be derived from Figure 5.21. The moment should be investigated further without the error due to the moment caused by the force. In Figure 5.21, it could be possible that all 3 DoFs follow the same curve.
More research needs to be done to investigate whether this newly proposed model is more accurate than the standard model.

6.3 Personal experience

During this thesis, I have learned a lot. Before I started my thesis, I was looking for a master's thesis where I would not only be working on simulations but also doing some physical exper-

iments and getting to build something. Fortunately, I found exactly that. The first discussions about the thesis were mostly focused on using the work that Kevin (my predecessor of the project) did on non-linear model predictive control and implementing it on the physical OmniMorph; the end result turned out to be different from this. I am very happy that the thesis turned out the way it did. Even though I did not work with it, I learned much about NMPC. I was able to help build an Omnimorph clone. I learned how to use the Genom software to work with UAVs. I performed experiments and used them to come up with useful results and data, which were used in a journal paper and a conference submission. In short, I got to experience the research process from start to finish. Not everything was perfect of course. At the start of the thesis, I felt like I took too long to read the research before beginning the work. When I started applying the theory, I grasped it much quicker than reading more research. There were also a few times when I lost my eye on the ball. I experienced the learning curve for the Genom as quite steep. I lost myself in it and spent too much time creating a custom model in Gazebo and making this work with MATLAB through Genom, while the only thing I needed to do was connect to the OmniMorph and set the velocity of the rotors. The same happened with the experiments. I have done many more tests than I really needed under the guise of: 'Now that I am here and doing this experiment, I might as well test this.' What I learned the most from this is that, before doing any tests or simulations, always analyze in detail what needs to be done to reach the goal.

A Full allocation matrix

$$\mathbf{F} = c_f \begin{bmatrix} -s_\alpha & 0 & 0 & s_\alpha \\ 0 & s_\alpha & -s_\alpha & 0 \\ c_\alpha & c_\alpha & c_\alpha & c_\alpha \\ Lc_\alpha - \frac{c_\tau s_\alpha}{c_f} & Lc_\alpha + Ls_\alpha & \frac{c_\tau s_\alpha}{c_f} - Lc_\alpha & -Lc_\alpha - Ls_\alpha \\ -Lc_\alpha - Ls_\alpha & Lc_\alpha + \frac{c_\tau s_\alpha}{c_f} & Lc_\alpha + Ls_\alpha & -Lc_\alpha - \frac{c_\tau s_\alpha}{c_f} \\ Ls_\alpha + \frac{c_\tau c_\alpha}{c_f} & Ls_\alpha - \frac{c_\tau c_\alpha}{c_f} & Ls_\alpha + \frac{c_\tau c_\alpha}{c_f} & Ls_\alpha - \frac{c_\tau c_\alpha}{c_f} \end{bmatrix}$$

$$\begin{bmatrix} s_\alpha & 0 & 0 & -s_\alpha \\ 0 & -s_\alpha & s_\alpha & 0 \\ c_\alpha & c_\alpha & c_\alpha & c_\alpha \\ Lc_\alpha + \frac{c_\tau s_\alpha}{c_f} & -Lc_\alpha - Ls_\alpha & -Lc_\alpha + Ls_\alpha & -Lc_\alpha - \frac{c_\tau s_\alpha}{c_f} \\ -Lc_\alpha - Ls_\alpha & \frac{c_\tau s_\alpha}{c_f} - Lc_\alpha & Lc_\alpha - \frac{c_\tau s_\alpha}{c_f} & Lc_\alpha + Ls_\alpha \\ \frac{c_\tau c_\alpha}{c_f} - Ls_\alpha & -Ls_\alpha - \frac{c_\tau c_\alpha}{c_f} - Ls_\alpha - \frac{c_\tau c_\alpha}{c_f} & \frac{c_\tau c_\alpha}{c_f} - Ls_\alpha & \end{bmatrix} \frac{\partial \mathbf{w}}{\partial \alpha} \tag{A.1}$$

B Hardware schematic

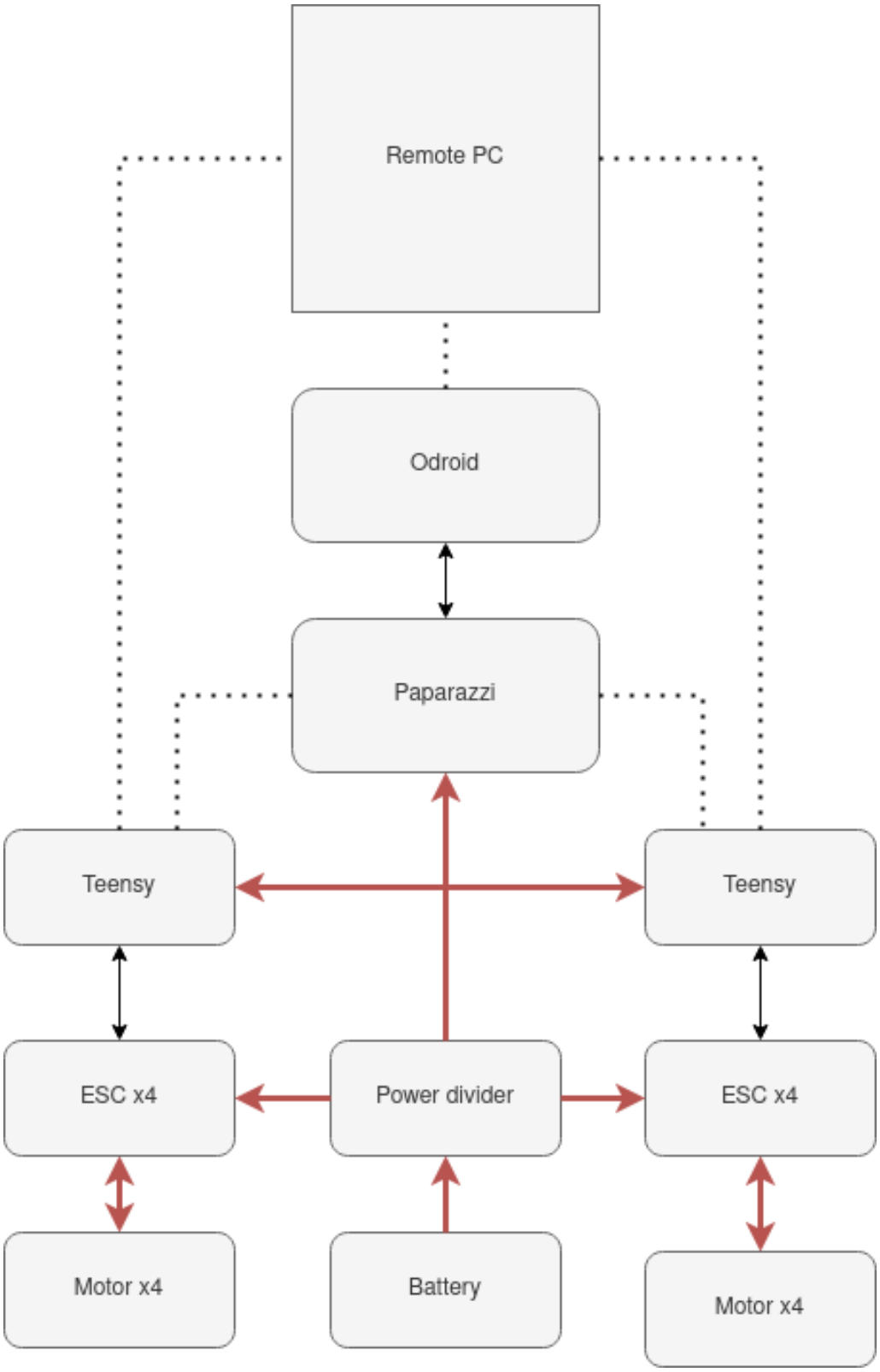

Figure B.1: Schematic representation of the OmniMorph with the power connections (red), data connections (black) and remote connections (dotted black).

C Genom architecture

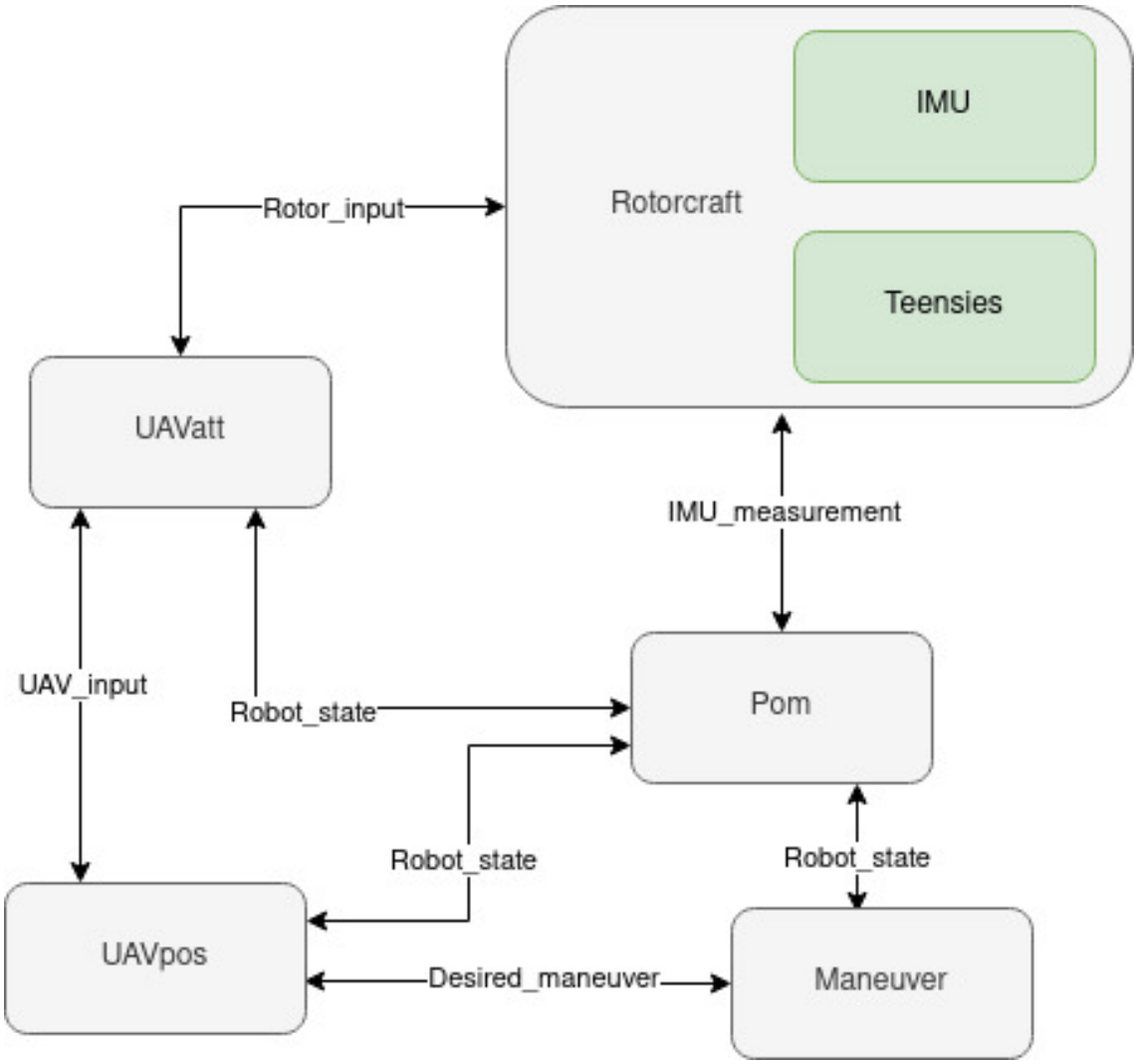

Figure C.1: Schematic representation of the Genom3 architecture components working together.

Bibliography

Aboudorra, Y., C. Gabellieri, R. Brantjes, Q. Sablé and A. Franchi (2024), Modelling, Analysis, and Control of OmniMorph: an Omnidirectional Morphing Multi-rotor UAV, **vol. 110**, no.1, p. 21, ISSN 1573-0409, doi:10.1007/s10846-024-02054-x.
https://doi.org/10.1007/s10846-024-02054-x

Aboudorra, Y., C. Gabellieri, Q. Sablé and A. Franchi (2023), Modelling, Analysis and Control of OmniMorph: an Omnidirectional Morphing Multi-rotor UAV, doi:10.48550/arXiv.2305.16871, arXiv:2305.16871 [cs, eess].
http://arxiv.org/abs/2305.16871

Allenspach, M., K. Bodie, M. Brunner, L. Rinsoz, Z. Taylor, M. Kamel, R. Siegwart and J. Nieto (2020), Design and optimal control of a tiltrotor micro aerial vehicle for efficient omnidirectional flight, **vol. 39**, no.10-11, pp. 1305–1325, ISSN 0278-3649, 1741-3176, doi:10.1177/0278364920943654, arXiv:2003.09512 [cs].
http://arxiv.org/abs/2003.09512

Bazzana, B., R. Brantjes, C. Gabellieri and A. Franchi (2024), An Experimentally Validated Model of the Propeller Force Accounting for Cross Influences on Multi-Rotor Aerial Systems, Submitted, Crete, Greece.

Brescianini, D. and R. D'Andrea (2018), An omni-directional multirotor vehicle, *Mechatronics*, **vol. 55**, pp. 76–93, ISSN 0957-4158, doi:10.1016/j.mechatronics.2018.08.005.
https://www.sciencedirect.com/science/article/pii/S0957415818301314

Chen, Y., M. Bruschetta, E. Picotti and A. Beghi (2019), MATMPC - A MATLAB Based Toolbox for Real-time Nonlinear Model Predictive Control, in *2019 18th European Control Conference (ECC)*, pp. 3365–3370, doi:10.23919/ECC.2019.8795788.
https://ieeexplore.ieee.org/document/8795788

Delbecq, S., M. Budinger, A. Ochotorena, A. Reysset and F. Defay (2020), Efficient sizing and optimization of multirotor drones based on scaling laws and similarity models, *Aerospace Science and Technology*, **vol. 102**, p. 105873, ISSN 1270-9638, doi:10.1016/j.ast.2020.105873.
https://www.sciencedirect.com/science/article/pii/S1270963820305551

Erdelj, M., E. Natalizio, K. R. Chowdhury and I. F. Akyildiz (2017), Help from the Sky: Leveraging UAVs for Disaster Management, **vol. 16**, no.1, pp. 24–32, ISSN 1558-2590, doi:10.1109/MPRV.2017.11, conference Name: IEEE Pervasive Computing.

Falanga, D., K. Kleber, S. Mintchev, D. Floreano and D. Scaramuzza (2019), The Foldable Drone: A Morphing Quadrotor That Can Squeeze and Fly, **vol. 4**, no.2, pp. 209–216, ISSN 2377-3766, 2377-3774, doi:10.1109/LRA.2018.2885575.
https://ieeexplore.ieee.org/document/8567932/

Franchi, A. (2023), 2022_CUAV_lecture_notes-v0.6-1.pdf.

Franchi, A., C. Secchi, M. Ryll, H. H. Bulthoff and P. R. Giordano (2012), Shared Control : Balancing Autonomy and Human Assistance with a Group of Quadrotor UAVs, **vol. 19**, no.3, pp. 57–68, ISSN 1558-223X, doi:10.1109/MRA.2012.2205625, conference Name: IEEE Robotics & Automation Magazine.

Hamandi, M., K. Sawant, M. Tognon and A. Franchi (2020), Omni-Plus-Seven (O7+): An Omnidirectional Aerial Prototype with a Minimal Number of Unidirectional Thrusters, in *2020 International Conference on Unmanned Aircraft Systems (ICUAS)*, IEEE, Athens, Greece, pp. 754–761, ISBN 978-1-72814-278-4, doi:10.1109/ICUAS48674.2020.9214065.
https://ieeexplore.ieee.org/document/9214065/

Hamandi, M., F. Usai, Q. Sablé, N. Staub, M. Tognon and A. Franchi (2021), Design of multirotor aerial vehicles: A taxonomy based on input allocation, **vol. 40**, no.8-9, pp. 1015–1044, ISSN 0278-3649, doi:10.1177/02783649211025998, publisher: SAGE Publications Ltd STM.
https://doi.org/10.1177/02783649211025998

Jeulink, K. (2023), The conception, development, implementation of a NMPC controller for the Omnimorph, publisher: University of Twente.
http://essay.utwente.nl/95053/

Kamel, M., S. Verling, O. Elkhatib, C. Sprecher, P. Wulkop, Z. Taylor, R. Siegwart and I. Gilitschenski (2018), The Voliro Omniorientational Hexacopter: An Agile and Maneuverable Tiltable-Rotor Aerial Vehicle, **vol. 25**, no.4, pp. 34–44, ISSN 1070-9932, 1558-223X, doi:10.1109/MRA.2018.2866758.
https://ieeexplore.ieee.org/document/8485627/

Khan, S., L. Aragão and J. Iriarte (2017), A UAV–lidar system to map Amazonian rainforest and its ancient landscape transformations, **vol. 38**, no.8-10, pp. 2313–2330, ISSN 0143-1161, doi:10.1080/01431161.2017.1295486, publisher: Taylor & Francis _eprint: https://doi.org/10.1080/01431161.2017.1295486.
https://doi.org/10.1080/01431161.2017.1295486

Kim, C., H. Lee, M. Jeong and H. Myung (2021), A Morphing Quadrotor that Can Optimize Morphology for Transportation, in *2021 IEEE/RSJ International Conference on Intelligent Robots and Systems (IROS)*, IEEE, Prague, Czech Republic, pp. 9683–9689, ISBN 978-1-66541-714-3, doi:10.1109/IROS51168.2021.9636558.
https://ieeexplore.ieee.org/document/9636558/

Leishman, J. G. (2016), *Principles of Helicopter Aerodynamics*, Cambridge University Press, 2nd edition, ISBN 978-1-107-01335-3, google-Books-ID: uscAMQAACAAJ.

Lottes, P., R. Khanna, J. Pfeifer, R. Siegwart and C. Stachniss (2017), UAV-based crop and weed classification for smart farming, in *2017 IEEE International Conference on Robotics and Automation (ICRA)*, pp. 3024–3031, doi:10.1109/ICRA.2017.7989347.

Mahony, R., V. Kumar and P. Corke (2012), Multirotor Aerial Vehicles: Modeling, Estimation, and Control of Quadrotor, **vol. 19**, no.3, pp. 20–32, ISSN 1558-223X, doi:10.1109/MRA.2012.2206474, conference Name: IEEE Robotics & Automation Magazine.
https://ieeexplore.ieee.org/document/6289431?denied=

Mallet, A., S. Fleury, M. Herrb, C. Pasteur and A. Degroote (2023), genom3 - Openrobots.
https://git.openrobots.org/projects/genom3

Mohammed, F., A. Idries, N. Mohamed, J. Al-Jaroodi and I. Jawhar (2014), UAVs for smart cities: Opportunities and challenges, in *2014 International Conference on Unmanned Aircraft Systems (ICUAS)*, pp. 267–273, doi:10.1109/ICUAS.2014.6842265.

Nikou, A., G. Gavridis and K. Kyriakopoulos (2015), Mechanical Design, Modelling and Control of a Novel Aerial Manipulator, doi:10.1109/ICRA.2015.7139851.

Ollero, A. (2023), Objectives.
https://aerial-core.eu/objectives/

Panagiotou, P. and K. Yakinthos (2020), Aerodynamic efficiency and performance enhancement of fixed-wing UAVs, *Aerospace Science and Technology*, **vol. 99**, p. 105575, ISSN 1270-9638, doi:10.1016/j.ast.2019.105575.
https://www.sciencedirect.com/science/article/pii/S1270963818324490

Park, S., J. Her, J. Kim and D. Lee (2016), Design, modeling and control of omni-directional aerial robot, in *2016 IEEE/RSJ International Conference on Intelligent Robots and Systems*

(IROS), pp. 1570–1575, doi:10.1109/IROS.2016.7759254, iSSN: 2153-0866.

Park, S., J. Lee, J. Ahn, M. Kim, J. Her, G.-H. Yang and D. Lee (2018), ODAR: Aerial Manipulation Platform Enabling Omnidirectional Wrench Generation, **vol. 23**, no.4, pp. 1907–1918, ISSN 1941-014X, doi:10.1109/TMECH.2018.2848255, conference Name: IEEE/ASME Transactions on Mechatronics.

Ryll, M., D. Bicego, M. Giurato, M. Lovera and A. Franchi (2022), FAST-Hex – A Morphing Hexarotor: Design, Mechanical Implementation, Control and Experimental Validation, **vol. 27**, no.3, pp. 1244–1255, ISSN 1083-4435, 1941-014X, doi:10.1109/TMECH.2021.3099197, arXiv:2004.06612 [cs, eess].
http://arxiv.org/abs/2004.06612

Ryll, M., H. H. Bulthoff and P. R. Giordano (2012), Modeling and control of a quadrotor UAV with tilting propellers, in *2012 IEEE International Conference on Robotics and Automation*, IEEE, St Paul, MN, USA, pp. 4606–4613, ISBN 978-1-4673-1405-3 978-1-4673-1403-9 978-1-4673-1578-4 978-1-4673-1404-6, doi:10.1109/ICRA.2012.6225129.
http://ieeexplore.ieee.org/document/6225129/

Saeed, A. S., A. B. Younes, C. Cai and G. Cai (2018), A survey of hybrid Unmanned Aerial Vehicles, *Progress in Aerospace Sciences*, **vol. 98**, pp. 91–105, ISSN 0376-0421, doi:10.1016/j.paerosci.2018.03.007.
https://www.sciencedirect.com/science/article/pii/S0376042117302233

Sastry, Zexiang Li, S. S. R. M. M. (2017), *A Mathematical Introduction to Robotic Manipulation*, CRC Press, Boca Raton, ISBN 978-1-315-13637-0, doi:10.1201/9781315136370.

Wargo, C. A., G. C. Church, J. Glaneueski and M. Strout (2014), Unmanned Aircraft Systems (UAS) research and future analysis, in *2014 IEEE Aerospace Conference*, pp. 1–16, doi:10.1109/AERO.2014.6836448, iSSN: 1095-323X.
https://ieeexplore.ieee.org/abstract/document/6836448

Zhao, M., T. Anzai, F. Shi, X. Chen, K. Okada and M. Inaba (2018), Design, Modeling, and Control of an Aerial Robot DRAGON: A Dual-Rotor-Embedded Multilink Robot With the Ability of Multi-Degree-of-Freedom Aerial Transformation, **vol. 3**, no.2, pp. 1176–1183, ISSN 2377-3766, 2377-3774, doi:10.1109/LRA.2018.2793344.
http://ieeexplore.ieee.org/document/8258850/